

Testing eternal inflation with the kinetic Sunyaev Zel'dovich effect

Pengjie Zhang^{a,b,c} and Matthew C. Johnson^{d,e}

^aCenter for Astronomy and Astrophysics, Department of Physics and Astronomy, Shanghai Jiao Tong University, 955 Jianchuan road, Shanghai, 200240, China

^bIFSA Collaborative Innovation Center, Shanghai Jiao Tong University, Shanghai 200240, China

^cKey Laboratory for Research in Galaxies and Cosmology, Shanghai Astronomical Observatory, 80 Nandan Road, Shanghai, 200030, China

^dDepartment of Physics and Astronomy, York University
Toronto, On, M3J 1P3, Canada

^ePerimeter Institute for Theoretical Physics
Waterloo, Ontario N2L 2Y5, Canada

E-mail: zhangpj@sjtu.edu.cn, mjohnson@perimeterinstitute.ca

Abstract. Perhaps the most controversial idea in modern cosmology is that our observable universe is contained within one bubble among many, all inhabiting the eternally inflating multiverse. One of the few way to test this idea is to look for evidence of the relic inhomogeneities left by the collisions between other bubbles and our own. Such relic inhomogeneities will induce a coherent bulk flow over Gpc scales. Therefore, bubble collisions leave unique imprints in the cosmic microwave background (CMB) through the kinetic Sunyaev Zel'dovich (kSZ) effect, temperature anisotropies induced by the scattering of photons from coherently moving free electrons in the diffuse intergalactic medium. The kSZ signature produced by bubble collisions has a unique directional dependence and is tightly correlated with the galaxy distribution; it can therefore be distinguished from other contributions to the CMB anisotropies. An important advantage of the kSZ signature is that it peaks on arcminute angular scales, where the limiting factors in making a detection are instrumental noise and foreground subtraction. This is in contrast to the collision signature in the primary CMB, which peaks on angular scales much larger than one degree, and whose detection is therefore limited by cosmic variance. In this paper, we examine the prospects for probing the inhomogeneities left by bubble collisions using the kSZ effect. We provide a forecast for detection using cross-correlations between CMB and galaxy surveys, finding that the detectability using the kSZ effect can be competitive with constraints from CMB temperature and polarization data.

Contents

1	Introduction	1
2	Cosmology in the aftermath of a bubble collision	4
3	The kinetic Sunyaev Zel’dovich effect generated by bubble collision	6
3.1	The effective velocity responsible for the kSZ effect	6
3.2	The kSZ auto power spectrum	13
3.3	The kSZ-large scale structure cross correlation	15
4	Using kSZ tomography to search for bubble collisions	17
4.1	The directional dependence of kSZ-galaxy cross correlation	17
4.2	The optimal weighting for bubble collisions	18
4.3	Comparison with constraints from the primary CMB	22
4.4	Constraints on the lagrangian underlying eternal inflation	23
5	Discussion and Summary	24
A	Linear Evolution of gravitational potential and velocity	25

1 Introduction

The idea that we might inhabit an eternally inflating multiverse is surely one of the most radical concepts to come out of modern physics. Although radical, accelerated expansion of the universe and spontaneous symmetry breaking, both observed phenomena in nature, are the necessary and sufficient ingredients. Once accelerated expansion driven by vacuum energy begins, an epoch known as inflation in the early universe, it is generically difficult to end globally. Instead, inflation ends only locally inside of bubbles which are formed only rarely via quantum mechanical effects. If bubbles are formed slower than the space between them is expanding, inflation cannot end globally, giving rise to the phenomenon of eternal inflation.

In this picture, our universe is housed within one bubble universe among many, perhaps each with different properties and cosmological histories (as motivated by the string theory landscape [1]). The Coleman de Luccia instanton [2–4] that mediates bubble nucleation dictates the symmetry of a one-bubble spacetime, giving rise to an open FRW universe in the bubble interior. If we live inside a bubble, a second epoch of slow-roll inflation is necessary to dilute curvature to observable levels and provide the seeds for structure formation [5–7].

Each bubble undergoes collisions with others [8], producing potentially observable wreckage [9]. Assessing the character of this wreckage and the probability of observing it has been the subject of a substantial body of work [10–43]. Given an underlying model consisting of a scalar field theory coupled to gravity, a full set of predictions can be made for the primordial metric fluctuations caused by a bubble collision [25, 29]. The symmetry of the collision spacetime forbids the production of gravitational waves [11, 12], and therefore the effects of a collision in any single-field model can be encoded in the primordial scalar comoving curvature perturbation. Bubble collisions can be mapped onto specific inhomogeneous initial

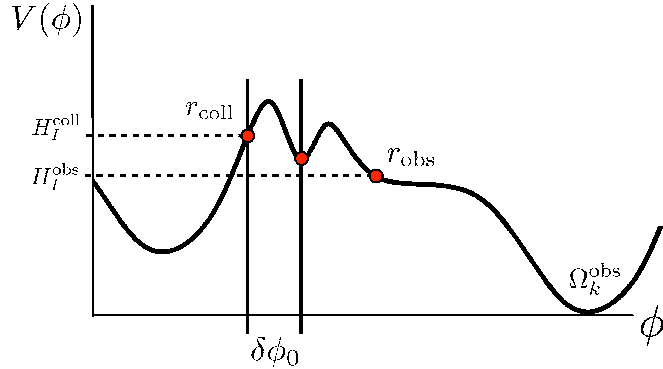


Figure 1. The scalar field potential underlying the bubble collision model.

conditions for slow-roll inflation inside of the bubble. Because the wreckage produced by bubble collisions is pre-inflationary, having the minimum number of inflationary e -folds is necessary for observable effects to be accessible today ¹.

Each collision is an event, and therefore can only affect regions in its causal future. The bubble interior is split into regions that are affected by the collision and regions that are not. Observers in the vicinity of this causal boundary have access to the most distinctive observational signatures; in the following we will focus on this class of observers. The first constraints on cosmic bubble collisions in the eternal inflation scenario were found by Feeney et al [46–49] using observations of the Cosmic Microwave Background (CMB) radiation made by the WMAP satellite [50]. This was followed up by the analysis of Osbourne et al [51, 52]. Neither of these analyses support the bubble collision hypothesis, placing a constraint on the possible models of eternal inflation. However, these analyses were performed with an incomplete understanding of the collision signature and the connection between the underlying theory and observable predictions. An analysis incorporating the improved predictions of [25, 29] is underway.

Because the dominant contribution to the CMB temperature anisotropies arises from the time of last scattering, it is not an ideal probe of inhomogeneity. CMB polarization probes the local temperature quadrupole observed by electrons, providing important additional information on inhomogeneities (see e.g. [53, 54]) and acting as an important discriminator between anisotropy and inhomogeneity. However, since the signature of a bubble collision is imprinted on the largest scales, cosmic variance is a significant impediment to placing stringent constraints on the bubble collision model. Can we ever hope to do better?

This paper explores the ability of another probe of large-scale inhomogeneities, the kinetic Sunyaev Zel’dovich (kSZ) effect [55], to test the bubble collision hypothesis. The kSZ effect is caused by the inverse Compton scattering of CMB photons by coherently moving free electrons. Its power to probe missing baryons, reionization and peculiar velocity at $\lesssim 100$ Mpc scale has been long recognized (e.g. [56–60]), and has been explored in CMB experiments such as ACT and SPT (e.g. [61, 62]). It can also be utilized to constrain dark matter-dark energy interaction [63] and modified gravity [64, 65]. Recently, a new regime of the kSZ effect generated by larger scale (\gtrsim Gpc) inhomogeneities has been realized and applied to probe dark flows [66–72], test the Copernican principle [73, 74], and constrain the

¹Various arguments may be advanced for the plausibility of this situation, see e.g. [44, 45]

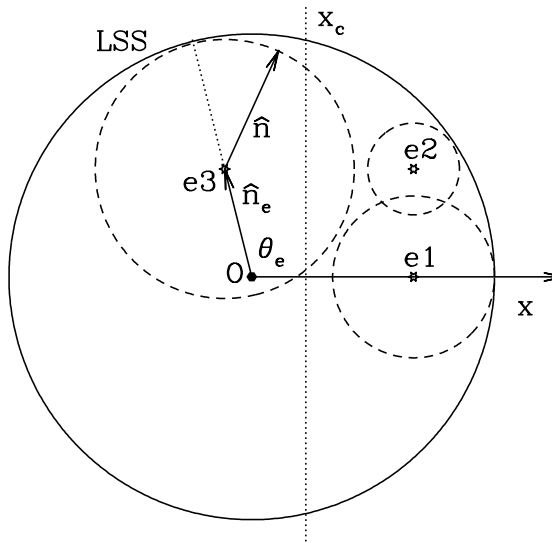


Figure 2. A schematic diagram of the kSZ effect in the collision spacetime. The causal boundary of the collision x_c is denoted by the dotted line (plane). The solid circle (sphere) is the last scattering surface (LSS) seen by us, and the dashed circles (spheres) are the LSS of several representative free electrons, labelled by “e1”, “e2” and “e3” respectively. These electrons see corresponding CMB dipoles on their LSS and have their own peculiar motion with respect to our CMB. In contrast to a single adiabatic superhorizon mode, the bubble collision generated perturbation induces $v_{\text{eff}} \neq 0$ and therefore induces a non-vanishing kSZ effect. Unlike the primary CMB fluctuation generated by bubble collision, which cover only a fraction of the sky, the kSZ effect generated by the bubble collision is spread over the whole 4π sky. For example, all electrons at a radius between “e3” and us (“O”) at all viewing angles can see the bubble collision through their LSS and hence generate a kSZ effect visible to us.

present day vacuum decay rate [75]. This paper presents its newest application.

The kSZ effect arises from scattering of CMB photons from free-electrons undergoing bulk motion in the late universe. The amplitude of the effect is proportional to the locally observed CMB dipole, and is therefore a sensitive measure of bulk velocities.² Horizon scale inhomogeneities generate bulk motions coherent over Gpc scales with characteristic directional dependence, and therefore, a distinctive kSZ signal. Note that this is a special class of kSZ signatures, distinctive from the conventional kSZ effect used to probe peculiar velocities on small scales.

The kSZ effect is a unique and powerful probe of horizon scale inhomogeneities, for a number of reasons.

1. Since the distance to the epoch of reionization (at $z \sim 6-10$) is very close to the distance to our horizon, free electrons probe much of the observable universe. Therefore the kSZ effect provides a unique opportunity to observe the universe from virtually every

²Although we do not consider it in this paper, polarization of the kSZ photons map the locally observed CMB quadrupole [76].

position inside of our horizon, and is sensitive to horizon scale inhomogeneities such as those generated by a bubble collision.

2. The kSZ signature is essentially a modulated re-mapping of the electron distribution to the CMB. Crucially, due to small scale inhomogeneities in the electron distribution, the power of the kSZ effect generated by horizon scale inhomogeneities peaks at arcminute angular scales.³ Hence, the kSZ effect promises to give constraints beyond the cosmic variance limited results obtained from the primary CMB only.
3. In contrast to the conventional kSZ effect, whose two-point cross correlation with the galaxy density field vanishes, the new kSZ effect is tightly correlated with the galaxy density field [67, 74]. Furthermore, the overall amplitude of the cross correlation has a unique directional modulation, depending on specific models of horizon scale inhomogeneities. Hence by specially designed cross correlation with galaxies, known as kSZ tomography [77], we can not only isolate it from other CMB components (primary CMB, other kSZ components, cosmic infrared background, etc), but also determine its redshift dependence.

The remainder of the paper is structured as follows. In Sec. 2 we discuss the predicted inhomogeneities produced by bubble collisions. Sec. 3 computes the kSZ signature expected for a general bubble collision. Sec. 4 estimates the capability of probing bubble collision using kSZ tomography, and makes a comparison with constraints obtained from the primary CMB. Finally, we discuss and summarize in Sec. 5.

2 Cosmology in the aftermath of a bubble collision

A model of eternal inflation is defined by a scalar field lagrangian, which by assumption has a metastable false vacuum and at least one true vacuum. Transitions from the false to the true vacuum are governed by the CDL instanton, which gives rise to bubbles of true vacuum nucleating in the false vacuum. The cosmological history inside the bubbles includes an epoch of cosmic inflation, and the $O(4)$ symmetry of the CDL instanton guarantees that a single bubble contains an infinite open Friedman Robertson Walker (FRW) universe. Focusing on a single bubble, which we hypothesize might contain our observable universe, additional bubbles forming from the false vacuum will collide with ours forming a fractal cluster of intersecting bubbles [8, 78]. In the limit where collisions are rare, they will lie outside of each other's horizon; we can therefore treat collisions on a pair-wise basis. The spacetime describing the collision between two bubbles has an $SO(2,1)$ symmetry [12], inherited from the symmetry of each of the colliding bubbles. Determining the precise outcome of a collision, and therefore the observable effects, has been examined using analytic and numerical methods. Recent efforts by Wainwright et al [25, 29] have established a connection between the primordial curvature perturbation and specific lagrangians, forming a first-principles derivation of the effects of bubble collisions in single field models. The conclusions of this work are as follows:

³Roughly speaking, fluctuation in such kSZ effect is proportional to the matter density fluctuation projected along some radial depth. Therefore the peak scale depends on the linear transfer function, σ_8 , relevant redshifts, and the projection length. For typical LCDM density fluctuation projected along Gpc radial depth, the typical peak scale is of the order one arcminute. This is numerically demonstrated in cases of dark flow induced kSZ effect [67]) and the kSZ effect discussed in this paper (Fig. 9).

- The boundary of the causal future of the collision splits the inner-bubble cosmology into two qualitatively different regions. This work considered observers who are in the vicinity of this boundary, reconstructing the perturbed FRW universe in this region in comoving gauge.
- On the scale of our observable universe, where spatial curvature can be neglected, the collision spacetime has approximate planar symmetry.
- Neglecting spatial curvature (at most a 1% effect), the perturbed FRW universe in Newtonian gauge is

$$ds^2 = -(1 + 2\Psi)dt^2 + a^2(t)(1 - 2\Psi)d\mathbf{x}^2 \quad (2.1)$$

with

$$\Psi_i(\mathbf{r}) \simeq \begin{cases} A(\tilde{x} - \tilde{x}_c) + B(\tilde{x} - \tilde{x}_c)^2, & \text{if } x \geq x_c \\ 0, & \text{if } x < x_c. \end{cases} \quad (2.2)$$

Here, we have fixed the collision direction to be along the x axis, and x_c is the location of the causal boundary. The prior probability distribution over x_c is flat over the size of the present day horizon. $\tilde{x} \equiv x/r_H$ and $r_H \equiv cH_0^{-1}$ is the present day Hubble radius (where c is the speed of light).

- A comparison between numerical and analytic methods in [29] showed that the coefficients A and B can be related to fundamental parameters of the scalar field lagrangian shown in Fig. 1 by ⁴:

$$A = \frac{2}{5} \sqrt{\frac{8\Omega_k^{\text{obs}}}{r_{\text{obs}}}} \frac{\delta\phi_0^{\text{coll}}}{M_{\text{pl}}} (1 - \cos \Delta x_{\text{sep}}) \quad (2.3)$$

$$B = \frac{2}{15} \Omega_k^{\text{obs}} \sqrt{\frac{r_{\text{coll}}}{r_{\text{obs}}}} \frac{H_I^{\text{coll}}}{H_I^{\text{obs}}} (1 - \cos \Delta x_{\text{sep}})^2$$

where $\delta\phi_0$ is the distance between the instanton endpoints connecting the false vacuum to the collision bubble interior, Ω_k^{obs} is the energy density in curvature in our own universe (constrained to be $\Omega_k^{\text{obs}} \lesssim 10^{-2}$), r_{obs} is the tensor to scalar ratio for inflation inside the observation bubble (constrained to be $r_{\text{obs}} \lesssim .1$), r_{coll} is the tensor to scalar ratio for inflation inside the collision bubble, H_I^{obs} is the Hubble scale during inflation inside the observation bubble, H_I^{coll} is the Hubble scale during inflation inside the collision bubble, and Δx_{sep} is the initial proper distance between the bubbles in the collision frame measured in terms of the false vacuum Hubble scale ($0 < \Delta x_{\text{sep}} < \pi$). By definition, $\delta\phi_0$ is positive for collisions between identical bubbles and negative for collisions between different bubbles. The prior probability distribution over initial separations Δx_{sep} is proportional to $\sin^3 \Delta x_{\text{sep}}$. We therefore expect $(1 - \cos \Delta x_{\text{sep}}) \sim \mathcal{O}(1)$. The analytic expression Eq. 2.3 assumes that slow-roll inflation is not disrupted by the collision, in which case H_I^{obs} is roughly constant everywhere in the collision spacetime during inflation. Complete disruption of inflation will occur when $\delta\phi_0^{\text{coll}}$ is comparable to the total field excursion during inflation inside the bubble. Using the Lyth Bound [?] ($\sqrt{r_{\text{obs}}} = \sqrt{0.01} \Delta\phi/M_{\text{pl}}$), we therefore conclude that Eq. 2.3 will be valid as long as $\delta\phi_0^{\text{coll}} < M_{\text{pl}} \sqrt{r_{\text{obs}}/0.01}$.

⁴Comparing with Ref. [29], a factor of 3/5 has been applied to convert between the Newtonian and comoving gauges, and we have converted our dimensionless measure of distance from the distance to the surface of last scattering to the size of the present day Hubble radius, introducing another factor of 3.

- We restrict ourselves to so-called native born observers [16], that is those who are comoving with respect to the unperturbed portion of the bubble. By definition, this restricts $x_c > 0$. There are also observers comoving with respect to the perturbed portion of the bubble. In the vicinity of x_c , these observers would have causal access to the collision boundary. Here, and also deep within the collision region, the dominant perturbation would be a quadratic curvature perturbation centred on the observer.

Cosmological datasets can be used to constrain the parameters in the template Eq. 2.2, which in turn constrains the underlying scalar field lagrangian through Eq. 2.3. We now turn to assessing the ability of the kSZ signature produced by bubble collisions to be used as such a probe.

3 The kinetic Sunyaev Zel’dovich effect generated by bubble collision

The curvature perturbation induced by bubble collisions gives rise to relative motion between matter in different regions of the Universe. Inverse Compton scattering off free electrons in relative motion induces temperature anisotropies in the observed CMB sky via the kSZ effect. The relevant induced temperature anisotropies are given by [55]

$$\frac{\Delta T}{T_{\text{CMB}}}(\hat{n}_e) = -\sigma_T \int_0^{\chi_{\text{re}}} d\chi_e a_e n_e(\chi(z_e)\hat{n}, z_e) \frac{v_{\text{eff}}(\hat{n}_e)}{c}. \quad (3.1)$$

The minus sign is chosen such that when an electron moves away from us ($v > 0$), the kSZ effect is negative. The vector \hat{n}_e points from us to the CMB sky, which is also the vector from us to the free electrons scattering CMB photons. The subscript “e” denotes properties of free electrons. $a_e = 1/(1+z_e)$ is the scale factor. χ_e is the comoving radial coordinate of free electrons, and $d\chi_e = cdz_e/H$. For a flat universe, χ_e coincides with the comoving angular diameter distance. n_e is the electron number density. v_{eff} is the effective velocity generating the kSZ effect, which we derive in detail below. Besides the peculiar velocity of electrons at redshift z and direction \hat{n}_e , it also takes into account the contribution from the intrinsic CMB dipole on the last scattering surface (LSS) of free electrons at different locations. This new contribution only exists in non-Copernican universes.

A schematic plot of the kSZ effect produced in the bubble collision spacetime is shown in Fig. 2. Since the distance to the reionization epoch at $z \sim 10$ is very close to the distance to our horizon, free electrons are essentially everywhere inside of our horizon. Each electron sees its own LSS, and combining all these LSS enables us to fairly sample all regions inside of our horizon. For example, the primary CMB along the line of sight from “O” to “e3” is not affected by the depicted bubble collision. Nevertheless, the kSZ effect generated by electrons located between “e3” and “O” allows us to infer the existence of a bubble collision along this line of sight. At fixed distance from us, the kSZ effect is confined within a disk. However, combining electrons from all distances spreads the effects of the bubble collision over the whole sky.

3.1 The effective velocity responsible for the kSZ effect

To calculate v_{eff} , we need to determine the evolution of the Newtonian potential and velocity. The perturbation induced by bubble collisions (Eq. 2.2) is a mixture of both superhorizon and subhorizon modes, with a dominant contribution from superhorizon modes. Subhorizon modes are further damped compared to superhorizon modes during cosmological evolution,

with the transfer function satisfying $T(k \gg 1/H)/T(k \ll 1/H) \ll 1$. Therefore we expect that the overall evolution of the potential and peculiar velocity can be approximated by that of the superhorizon modes, which are scale independent, and have analytical expressions (e.g. [79]). We outline this computation in Appendix A. To test this approximation, we numerically compute the potential and peculiar velocity by solving the Boltzmann equations for radiation and cold dark matter (CDM) in a flat universe. We confirm that the superhorizon approximation works very well (Fig. 17, Appendix A). Including the sub-horizon evolution acts to slightly smooth the causal boundary at x_c , a consequence of the damping of sub-horizon (small scale) modes. We neglect this effect, as well as the baryon-photon coupling before last scattering⁵. Hereafter we will adopt the superhorizon approximation and use the analytic expressions in Appendix A to calculate the kSZ effect induced by bubble collision.

The potential Ψ at late times follows the same form as Eq. 2.2 but with a scale-invariant growth factor $D_\Psi(a)$ (given by Eq. A.6):

$$\Psi(\mathbf{r}, a) = D_\Psi(a)\Psi_i(\mathbf{r}) . \quad (3.2)$$

For the velocity field, only the x-component is non-zero. It is well described by

$$v_x(\mathbf{r}, a) = -D_v(a)r_H^{-1} \times \begin{cases} A + 2B(\tilde{x} - \tilde{x}_c), & \text{if } x \geq x_c \\ 0, & \text{if } x < x_c . \end{cases} \quad (3.3)$$

The linear velocity growth factor D_v is given by Eq. A.8. Throughout the paper we will discuss two limiting cases with $(A, B) = (\neq 0, 0)$ (case A) and $(A, B) = (0, \neq 0)$ (case B).

The effective velocity in Eq. 3.1 is related to the CMB dipole observed by a freely falling electron via

$$v_{\text{eff}}(\hat{n}_e) = \frac{3}{4\pi} \int_{4\pi} d^2\hat{n} \Theta(\mathbf{r}_{\text{dec}}) (\hat{n} \cdot \hat{n}_e) . \quad (3.4)$$

Here $\cos\theta \equiv \hat{n} \cdot \hat{n}_e$ and the unit vector \hat{n} points from the electrons to their LSS. $\mathbf{r}_{\text{dec}} = \chi_e \hat{n}_e + \Delta\chi_{\text{dec}} \hat{n}$. Here $\chi_e \equiv \chi(z_e)$ is the distance from us to free electrons, and $\Delta\chi_{\text{dec}} \equiv \chi(z_{\text{dec}}) - \chi_e$ is the distance from the electrons to their LSS. The geometry is shown in Fig. 2. The effective velocity has three contributions,

$$v_{\text{eff}}(\hat{n}_e) = v_{\text{eff},\text{SW}} + v_{\text{eff},\text{Doppler}} + v_{\text{eff},\text{ISW}} . \quad (3.5)$$

These contributions come from the Sachs-Wolfe (SW) effect generated by the gravitational potential on the LSS, the Doppler effect due to peculiar motion of photons on the LSS and peculiar motion of electrons at redshift z_e , and the integrated Sachs-Wolfe (ISW) effect [80], respectively. For a freely falling electron at redshift z_e and position $\mathbf{r}_e \equiv \chi_e \hat{n}_e$, the CMB temperature it sees along the direction \hat{n} is

$$\Theta(\hat{n}) = \Theta_{\text{SW}}(\hat{n}) + \Theta_{\text{Doppler}}(\hat{n}) + \Theta_{\text{ISW}}(\hat{n}) . \quad (3.6)$$

We follow [79] to evaluate the above terms. The SW term is

$$\Theta_{\text{SW}}(\hat{n}) = \left[2 - \frac{5}{3} \frac{9/10}{D_\Phi(a_{\text{dec}})} \right] \Psi(\mathbf{r}_{\text{dec}}, a_{\text{dec}}) = \left[2 - \frac{5}{3} \frac{9/10}{D_\Phi(a_{\text{dec}})} \right] D_\Psi(a_{\text{dec}})\Psi_i(\mathbf{r}_{\text{dec}}) . \quad (3.7)$$

⁵This gives rise to the ‘‘cosmic wakes’’ described in Ref. [23], and may add structure to baryon peculiar velocities on BAO scales in the vicinity of the causal boundary beyond what is considered here. We do not expect such signatures to significantly alter our results.

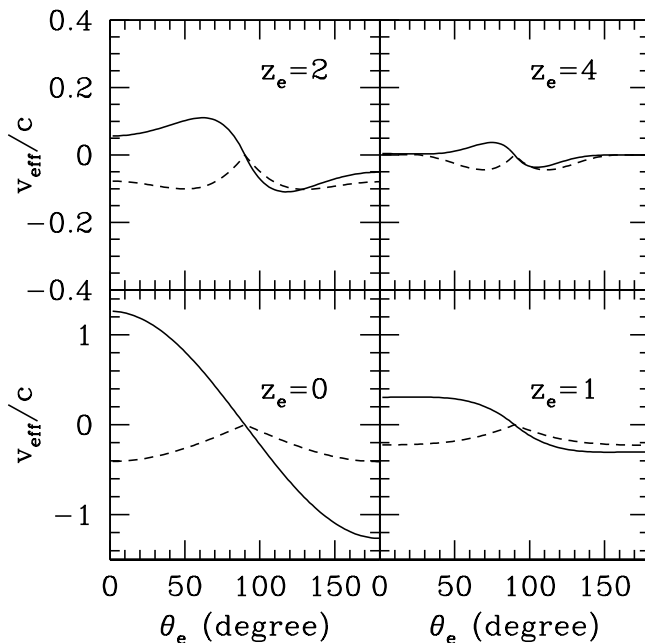


Figure 3. The effective peculiar velocity that generates the kSZ effect, for $z_c = 0$. Electrons sit at $z_e = 0, 1, 2, 4$ respectively. The solid lines have $B = 1$ and $A = 0$. The dash lines have $A = 1$ and $B = 0$. z_c is the closest redshift to the causal boundary of the collision. Due to the azimuthal symmetry of the initial perturbation, $v_{\text{eff}} = 0$ when $\theta_e = \pi/2$. For $A = 1$ and $B = 0$, we have the analytical expression at $z_e = 0$: $v_{\text{eff}} = v_e \cos(\theta_e)$ when $\theta_e > \pi/2$ and $-v_e \cos(\theta_e)$ when $\theta_e < \pi/2$. The value of v_e is given in Fig. 17. For $z_e = 4$, v_{eff} approaches zero when $\theta_e \rightarrow 0$ or $\theta_e \rightarrow \pi$, but for different reasons. The reason it approaches zero when $\theta_e \rightarrow \pi$ is that the electrons and their last scattering spheres are located in unperturbed regions. The reason it approaches zero when $\theta_e \rightarrow 0$ is due to the cancellation of SW, ISW and Doppler components [79].

Here we have neglected the impact of $\Psi(\mathbf{r}_e, a_e)$ since it does not cause an observable effect. The Doppler effect has two contributions with opposite sign,

$$\Theta_{\text{Doppler}}(\hat{n}) = \hat{n} \cdot [\mathbf{v}(\mathbf{r}_e, a_e) - \mathbf{v}(\mathbf{r}_{\text{dec}}, a_{\text{dec}})] = \hat{n} \cdot [D_v(a_{\text{dec}})\nabla\Psi_i(\mathbf{r}_{\text{dec}}) - D_v(a_e)\nabla\Psi_i(\mathbf{r}_e)] \quad (3.8)$$

The ISW effect is given by

$$\Theta_{\text{ISW}}(\hat{n}) = 2 \int_{a_{\text{dec}}}^{a_e} \frac{d\Psi}{da}(\mathbf{r}(a), a) da = 2 \int_{a_{\text{dec}}}^{a_e} \frac{dD\Psi}{da} \Psi_i(\mathbf{r}(a)) da . \quad (3.9)$$

Here, $\mathbf{r}(a) = \mathbf{r}_e + \Delta\chi\hat{n}$. $\Delta\chi(a) \equiv \int_a^{a_e} da/a^2 H$. So $\Delta\chi_{\text{dec}} = \Delta\chi(a_{\text{dec}})$.

Before proceeding, there is an important issue to clarify. For adiabatic perturbations in a flat universe, and in the limit of constant gradient in the gravitational potential corresponding to a very superhorizon mode, the three contributions (SW, Doppler and ISW) cancel exactly ($\Theta(\hat{n}) = 0$) [79, 81–83]. Therefore $v_{\text{eff}} = 0$ (vanishing CMB dipole). This was first found by [81–83] for a $\Omega_m = 1$ Einstein-de Sitter universe. Erickcek et al. [79] proved that it also holds in an Λ CDM universe with radiation and an CDM universe with smooth dark energy and radiation. They further argue that this should be a generic feature for adiabatic

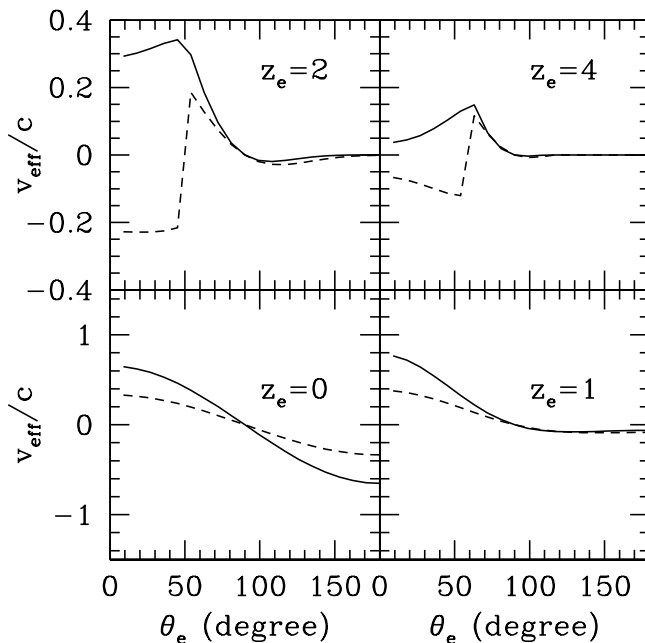


Figure 4. Same as Fig. 3, but for $z_c = 1$. Notice that when $\theta_e \rightarrow \pi$ and $z_e \gtrsim 2$, the electrons and their last scattering spheres are located in unperturbed regions and hence $v_{\text{eff}} \rightarrow 0$. The sharp decrease at $\theta_e \simeq 50^\circ$ for $z_e = 2$ (and at $\theta_e \simeq 60^\circ$ for $z_e = 4$) and $B = 0$ is caused by the discontinuity of velocity at the edge of bubble collision. This sharp feature shows up when $z_e > z_c$. $v_{\text{eff}}(\hat{n})$ shows a rich dependence on the observation angle, a precious property for clean extraction from an otherwise noisy CMB sky.

superhorizon modes so that the cancellation holds in all flat cosmologies. For these cases, the kSZ effect vanishes. Fortunately for the bubble collision generated inhomogeneities, the exact cancellation no longer works, for two reasons. First, the curvature perturbation has a quadratic term, and hence a spatially varying gradient. So in general $v_{\text{eff}} \neq 0$. Second, even if the quadratic term vanishes ($B = 0$), due to the discontinuity in gradient on the edge of a bubble collision, $v_{\text{eff}} \neq 0$ for electrons whose LSSs are not completely inside of the region perturbed by bubble collision (e.g. at position “e3” in Fig. 2). Although electrons whose LSS are completely inside of the region affected by bubble collision (e.g. “e1” and “e2” in Fig. 2) can have $v_{\text{eff}} = 0$ for $B = 0$, overall $v_{\text{eff}} \neq 0$ and we expect a non-vanishing kSZ effect.

The azimuthal symmetry of the collision spacetime allows us to choose the parameterization

$$\begin{aligned} \hat{n}_e &\equiv (\cos \theta_e, \sin \theta_e, 0) , \\ \hat{n} &\equiv (\cos \theta, \sin \theta \cos \varphi, \sin \theta \sin \varphi) . \end{aligned} \quad (3.10)$$

The integral over φ in Eq. 3.4 is always $[0, 2\pi]$. To evaluate the integral over θ in Eq. 3.4, we must consider three cases:

1. $\chi_e \cos \theta_e + \Delta \chi_{\text{dec}} < x_c$. The LSS of the electron is outside of the region affected by the bubble collision and therefore $v_{\text{eff}} = 0$.

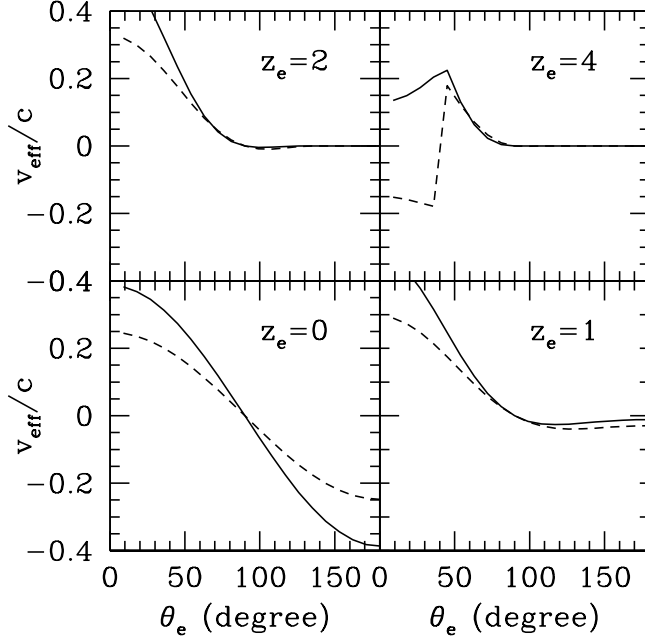


Figure 5. Same as Fig. 3, but for $z_c = 2$. Notice that, for $z_e = 0$, v_{eff} is anti-symmetric under the operation $\theta_e \leftrightarrow \pi - \theta_e$, a direct result of azimuthal symmetry. The only exception is when $z_c = 0$ and $B = 0$ where the anti-symmetry is reversed to symmetry, caused by the sharp transition in the velocity field at $z_e = z_c = 0$ (Fig. 3).

2. $\chi_e \cos \theta_e - \Delta \chi_{\text{dec}} > x_c$. The LSS of the electron is completely inside of the region affected by the bubble collision. So the integral is over $\theta \in [0, \pi]$.
3. $\chi_e \cos \theta_e - \Delta \chi_{\text{dec}} < x_c$ & $\chi_e \cos \theta_e + \Delta \chi_{\text{dec}} > x_c$. Only part of the LSS is inside of the region affected by the bubble collision. Therefore the integral is over $[0, \theta_c]$. θ_c is the solution of θ to $\chi_e \cos \theta_e + \Delta \chi_{\text{dec}} \cos \theta = x_c$, namely $\cos \theta_c = (x_c - \chi_e \cos \theta_e) / \Delta \chi_{\text{dec}}$.

For cases 2 and 3, we obtain

$$v_{\text{eff,SW}} = \left[2 - \frac{5}{3} \frac{9/10}{D_{\Phi}(a_{\text{dec}})} \right] D_{\Psi}(a_{\text{dec}}) \times \frac{3}{2} \cos \theta_e \left[A \left((\chi_e \cos \theta_e - x_c) \frac{\cos^2 \theta}{2} + \Delta \chi_{\text{dec}} \frac{\cos^3 \theta}{3} \right) + B \left((\chi_e \cos \theta_e - x_c)^2 \frac{\cos^2 \theta}{2} + (\chi_e \cos \theta_e - x_c) \Delta \chi_{\text{dec}} \frac{2 \cos^3 \theta}{3} + \frac{\Delta \chi_{\text{dec}}^2 \cos^4 \theta}{4} \right) \right]_{\theta_c}^0 \quad (3.11)$$

$$v_{\text{eff,Doppler}} = \mathbf{v}(\mathbf{r}_e, a_e) \cdot \hat{\mathbf{n}}_e + \frac{3}{2} \cos \theta_e D_v(a_{\text{dec}}) \times \left[\frac{A \cos^3 \theta}{3} + \frac{2B(\chi_e \cos \theta_e - x_c) \cos^3 \theta}{3} + \frac{B \Delta \chi_{\text{dec}} \cos^4 \theta}{2} \right]_{\theta_c}^0. \quad (3.12)$$

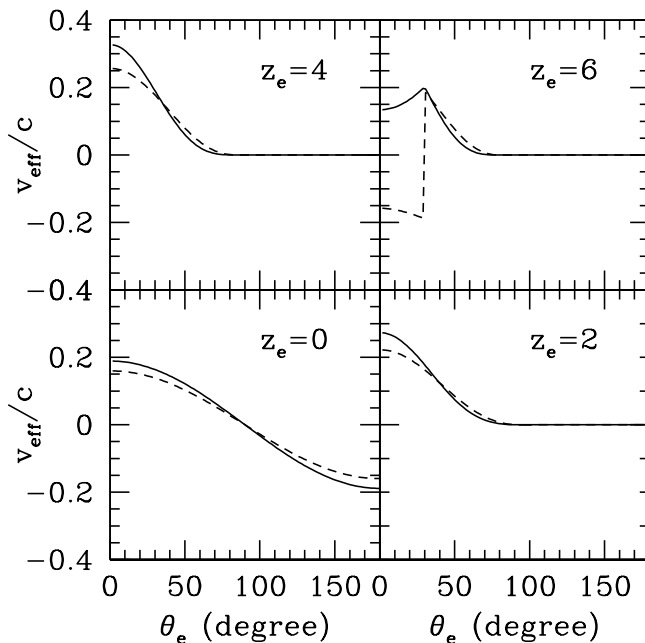


Figure 6. Similar to Fig. 3, but for $z_c = 4$ and $z_e = 0, 2, 4, 6$ instead. The two cases of initial fluctuations produce similar v_{eff} at $z_e \lesssim z_c$, but this is a coincidence. At higher z_e , the two cases differ significantly. In particular, the sharp transition at $z_e = 6$ and $B = 0$ shown in Fig. 5 shows up here when $z_e = 6$. These electrons sit at the edge of bubble collision, satisfying $\chi_e \cos \theta_e = x_c \equiv \chi(z_c)$.

To calculate the ISW effect, we just need to replace Ψ_i in Eq. 3.9 by

$$\begin{aligned} \Psi_i \rightarrow & \frac{3 \cos \theta_e}{2} \left[A \left((\chi_e \cos \theta_e - x_c) \frac{\cos^2 \theta}{2} + \Delta \chi \frac{\cos^2 \theta}{3} \right) \right. \\ & \left. + B \left((\chi_e \cos \theta_e - x_c)^2 \frac{\cos^2 \theta}{2} + (\chi_e \cos \theta_e - x_c) \Delta \chi \frac{2 \cos^3 \theta}{3} + \frac{\Delta \chi^2 \cos^4 \theta}{4} \right) \right]_{\theta_c}^0. \end{aligned}$$

Notice that now $\cos \theta_c = (x_c - \chi_e \cos \theta_e) / \Delta \chi(a)$. In the limit of no intrinsic CMB dipole, we recover the conventional kSZ effect with $v_{\text{eff}} = \mathbf{v}(\mathbf{r}_e, a_e) \cdot \hat{n}_e$.

Fig. 3, 4, 5, 6, 7 & 8 show the values of v_{eff} and its dependence on θ_e , z_e , z_c , A and B . z_c is the minimum redshift to the edge of bubble collision, with $x_c = \chi(z_c)$. For quick reference, we plot the x_c - z_c relation in Fig. 16. As expected, v_{eff}/c is in general of the same order as A and B . Nevertheless, numerical results show that the maximum value of v_{eff}/c is often smaller than A or B by a factor of a few to 10. This is likely caused by incomplete cancellation between the SW, ISW and the Doppler effect [79, 81–83].

We show v_{eff} as a function of θ_e for different values of $z_e = 0, 1, 2$ & 4, and $z_c = 0$ (Fig. 3), $z_c = 1$ (Fig. 4), $z_c = 2$ (Fig. 5) and $z_c = 4$ (Fig. 6). v_{eff} shows unique directional dependence on θ_e , which in general can not be mimicked by conventional sources and contaminants. Furthermore, such directional dependence relies on z_e , z_c , A and B in complicated and different ways. For the purpose of extracting the bubble collision generated

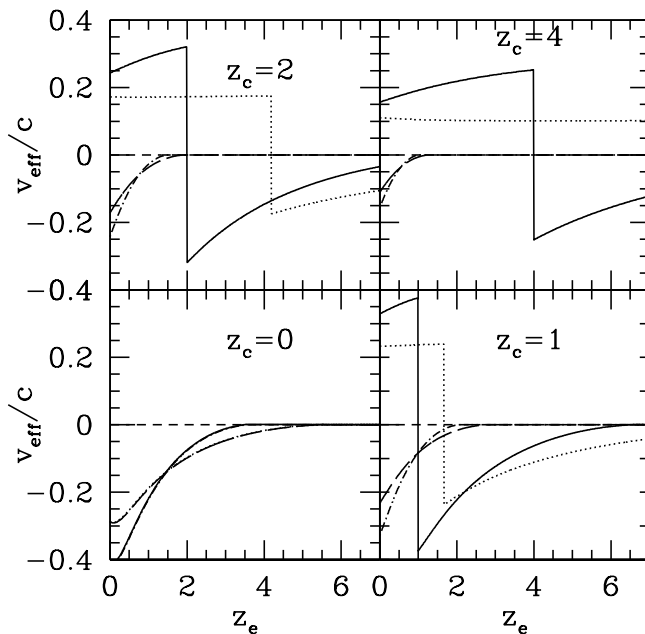


Figure 7. The $v_{\text{eff}}-z_e$ relation for $A = 1$, $B = 0$ and electrons with $\theta_e = 0$ (solid lines), $\pi/4$ (dot lines), $\pi/2$ (dash lines), $3\pi/4$ (long dash lines), and π (dot-short dash lines), respectively. Notice that due to the azimuthal symmetry, $v_{\text{eff}}(\theta_e = \pi/2) = 0$. For $z_c = 0$, the lines with $\theta_e = 0$ overlap with those for $\theta_e = \pi$. This can be understood by the result that $v_{\text{eff}} = 0$ if $\Psi = A(x - x_c)$ without the causal boundary at $x = x_c$ [79]. Also for this reason, the lines $\theta_e = \pi/4$ overlap with those for $\theta_e = 3\pi/4$. An interesting behavior is that for $\theta_e = 0$, $v_{\text{eff}}(z_e)$ is nearly a constant when $z_e < z_c$.

kSZ effect from otherwise overwhelming contaminants and constraining collision parameters (A , B and $x_c \equiv \chi(z_c)$), this is good news.

Although in general these features can only be obtained numerically, some of them can be understood analytically.

1. For example, due to the azimuthal symmetry, $v_{\text{eff}}(\theta_e = \pi/2) = 0$. This holds for all values of z_e , z_c , A , B and x_c . Also for this symmetry, $v_{\text{eff}}(\pi - \theta_e) = -v_{\text{eff}}(\theta_e)$ when $z_e = 0$ and $z_c > 0$. When $z_c = 0$, this symmetry still holds for the case B. But for case A, due to the discontinuity in the velocity field at $z_e = 0$, we have $v_{\text{eff}}(\pi - \theta_e) = v_{\text{eff}}(\theta_e)$ instead.
2. For case A with $z_c = 0$ and $z_e = 0$, we have $v_{\text{eff}}(\theta_e) = v_e(z = 0) \cos \theta_e$ when $\theta_e > \pi/2$, and $v_{\text{eff}}(\theta_e) = -v_e(z = 0) \cos \theta_e$ when $\theta_e < \pi/2$. The value of $v_e(z = 0)$ is given in Fig. 17.
3. For some combinations of z_c , z_e and θ_e , the LSS of electrons is located outside of the region affected by the bubble collision. Therefore we have $v_{\text{eff}} = 0$ there.
4. For some other combinations of z_c , z_e and θ_e , the LSS of electrons are located completely inside of the region affected by the bubble collision. Therefore we have $v_{\text{eff}} = 0$ for case A, due to the cancellation of the SW, Doppler and ISW effect [79, 81–83].

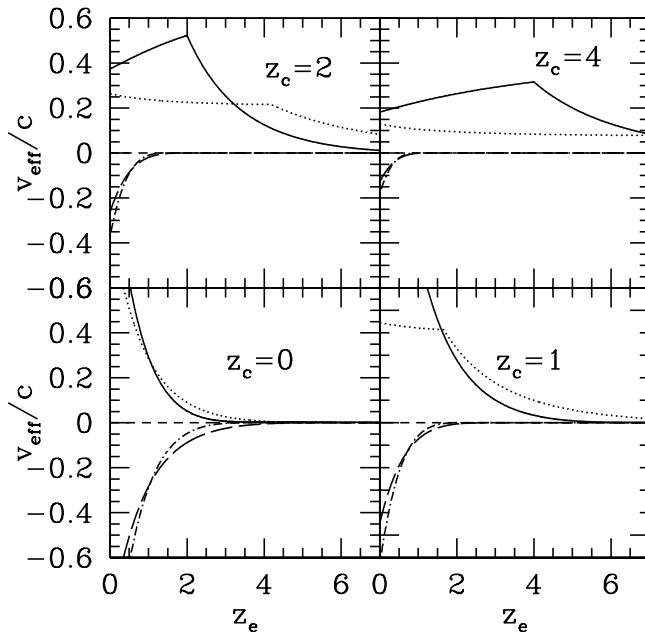


Figure 8. Similar to Fig. 7, but for the $v_{\text{eff}}-z_e$ relation with $B = 1$ and $A = 0$.

5. For case A, there is often a discontinuity in $v_{\text{eff}} - \theta_e$. This happens when electrons with varying θ_e cross the causal boundary of collision, where the velocity is discontinuous.

It is also useful to examine the dependence of v_{eff} on z_e for fixed θ_e . This, together with $a\bar{n}_e \propto (1+z)^2$ and the evolution of electron number overdensity, determines the contribution of electrons at a given redshift to the kSZ effect. Therefore we plot the $v_{\text{eff}}-z_e$ relation in Fig. 7 & 8, for various $\theta_e = 0, \pi/4, \pi/2, 3\pi/4$ & π . As expected, v_{eff} along a fixed line of sight is coherent over Gpc scales. It thus avoids cancellation of velocity of different signs in the conventional kinetic SZ effect [56]. Also for this reason, the kSZ-galaxy number density cross correlation does not vanish, in contrast to the vanishing cross correlation between the conventional kSZ and galaxies (e.g. Fig. 1, [77]).

3.2 The kSZ auto power spectrum

The kSZ auto power spectrum induced by a bubble collision is extremely small. For an order of magnitude estimate, we can compute

$$\Delta T/T \sim \tau(v_{\text{eff}}/c)\delta_e \quad (3.13)$$

with $\tau \sim 0.01$ and density fluctuation $\delta_e \sim 0.1$ at arcminute scales where the signal will peak. From the previous section, the maximum value of v_{eff}/c is roughly set by the magnitude of A and/or B . As we discuss in more detail in Sec. 4.3, existing constraints from the collision signature in the primary CMB are roughly $A < 10^{-4}$ (B has yet to be constrained in the primary CMB). The level of the signature in kSZ power spectrum is therefore $\Delta T^2 \lesssim 1\mu\text{K}^2$ (for the unrealistic values $A, B \sim 10^{-3}$) to $\Delta T^2 \lesssim .01\mu\text{K}^2$ (at the upper bounds allowed by the primary CMB). This is far smaller than the most recent measurement of the kSZ power

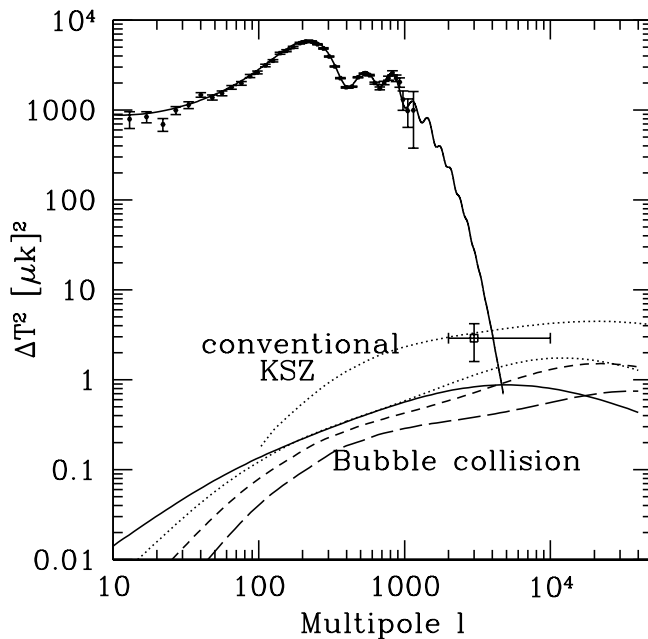


Figure 9. The kSZ power spectrum for $B = 10^{-3}$ along the line of sight towards the centre of the bubble collision. Solid, dot, shot dash and long dash lines have $z_c = 0, 1, 2, 4$ respectively. The generated kSZ effect is sub-dominant to the conventional kSZ effect calculated using the model of [59]. It is also well below the measured band-power of the conventional kSZ effect at $\ell \sim 3000$ ($2000 < \ell < 10000$) by SPT [62]. Given the existence of overwhelming contamination from a combination of the primary CMB, conventional kSZ and cosmic infrared background, it is infeasible to detect bubble collision through a measurement of the kSZ auto power spectrum.

spectrum from the South Pole Telescope [84] (SPT) which finds the bandpower $\Delta T^2 = 2.9 \pm 1.3 \mu\text{K}^2$ at $\ell = 3000$, notwithstanding the primary CMB, thermal SZ, cosmic infrared background, and instrumental noise.

To confirm this rough estimate, we can perform a more accurate computation following the derivation of the dark flow induced kSZ effect outlined in Ref. [67]. Using the Limber approximation, the kSZ power spectrum in the \hat{n}_e direction is given by,

$$\Delta T_{\text{kSZ}}^2(\ell, \hat{n}_e) = (0.167 \mu\text{k})^2 \frac{\pi}{\ell} \int_0^{z_{\text{re}}} \Delta_e^2 \left(\frac{\ell}{\chi_e}, z_e \right) \left[\frac{v_{\text{eff}}(\hat{n}_e, z_e)}{10 \text{km/s}} \right]^2 (1 + z_e)^4 \chi_e d\chi_e. \quad (3.14)$$

$\Delta_e^2(k, z)$ is the power spectrum (variance) of the electron number overdensity at redshift z . In principle it has contributions both from the conventional primordial fluctuation and from the bubble collision. Observationally we know that the first dominates otherwise the concordance ΛCDM cosmology would not work so well. Therefore we will approximate Δ_e^2 as that predicted by the standard ΛCDM cosmology.⁶

Fig. 9 shows the numerical results for the kSZ auto power spectrum for case B with $B = 10^{-3}$ toward the center of the bubble collision. It peaks at $\ell \sim 10^4$, with peak amplitude $\lesssim 1 \mu\text{K}^2$. It is subdominant to the conventional kSZ effect by a factor of a few at all angular

⁶We have numerically verified that this is indeed the case for interesting values of $A, B \lesssim 10^{-3}$.

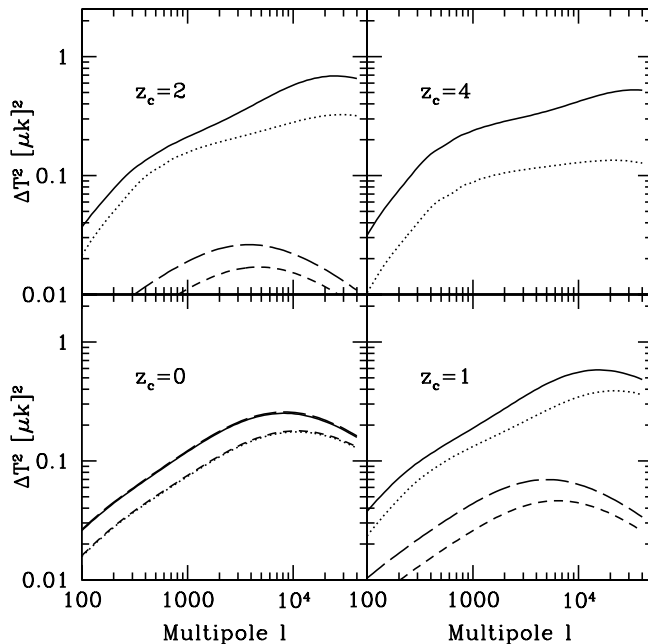


Figure 10. The kSZ power spectrum for $A = 10^{-3}$. Solid, dot, shot dash and long dash lines have $\theta_e = 0^\circ, 45^\circ, 135^\circ, 180^\circ$ respectively. Notice that when $\theta_e = 90^\circ$, the kSZ effect vanishes.

scales. It is also subdominant to the lensed primary CMB at $\ell \lesssim 4000$. Fig. 10 & 11 show that this sub-dominance holds for other lines of sight and for both case A and B, with $A, B = 10^{-3}$ respectively. The auto power spectrum for other values of A, B scales as $(A, B/10^{-3})^2$. Since only $A, B \lesssim 10^{-4}$ is allowed by constraints from primary CMB, the kSZ effect induced by bubble collisions cannot be detected in the temperature power spectrum. Nevertheless, we now show that kSZ tomography, namely the kSZ-large scale structure cross correlation, is a promising probe for bubble collisions.

3.3 The kSZ-large scale structure cross correlation

Although the kSZ signature of bubble collisions in the temperature power spectrum is hopelessly buried, kSZ tomography can be used to boost the signal by specifically designed weighted cross correlations of CMB temperature with galaxies [67, 77, 85, 86]. A schematic is shown in Fig. 12; in a set of redshift bins the kSZ effect caused by bubble collisions is a modulated map of the galaxy distribution onto CMB temperature. This technique has been applied to WMAP-SDSS [69] and Planck-SDSS (Li, Zhang & Jing, submitted to ApJ) to search for the dark flow induced kSZ effect. In addition to correlations with the distribution of galaxies, one also expects a tight correlation between the kSZ effect in the CMB and the lensing field (e.g. [87]) or other tracers of large scale structure such as the 21cm intensity maps. For brevity, we focus in this work on cross correlating with galaxies.

For galaxies in a redshift bin $[z_1, z_2]$, the surface overdensity is $\delta\Sigma = \int_{z_1}^{z_2} \bar{n}_g \delta_g dz$. Here, \bar{n}_g is normalized such that $\int_{z_1}^{z_2} \bar{n}_g dz = 1$. We consider a typical bin size of $\Delta z \equiv z_2 - z_1 \sim 0.2$. For redshift bins defined by photometric redshift, we shall take the broadening of redshift width by photo-z error into account. $v_{\text{eff}}(\hat{n})$ only varies slowly with sky direction. So to

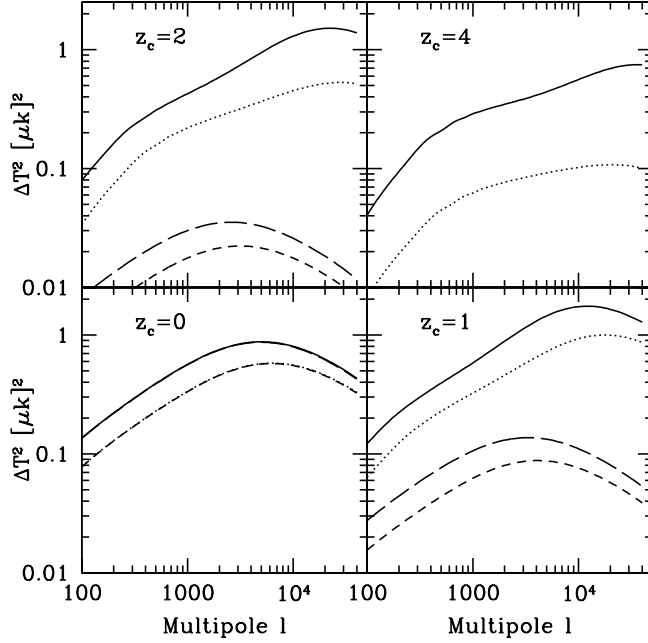


Figure 11. The kSZ power spectrum for $B = 10^{-3}$. Solid, dot, shot dash and long dash lines have $\theta_e = 0^\circ, 45^\circ, 135^\circ, 180^\circ$ respectively. Notice that when $\theta_e = 90^\circ$, the kSZ effect vanishes.

excellent approximation, over degree scales, it can be treated as constant. Hence for a degree-sized patch centered on the direction \hat{n}_P , the cross correlation of galaxies with kSZ can be well approximated by [67]

$$\frac{\ell^2}{2\pi} C_{Tg}(\ell|\hat{n}_P) = -\frac{\pi}{\ell} \int_{z_1}^{z_2} \frac{\bar{n}_e \sigma_{TA} a}{c} \Delta_{eg}^2(k, z) \bar{n}_g(z) \chi(z) v_{\text{eff}}(\hat{n}_P, z) dz. \quad (3.15)$$

Here the electron density-galaxy density power spectrum (variance) $\Delta_{eg}^2(k, z)$ is evaluated at $k = \ell/\chi(z)$, following the Limber approximation. We can define a temperature fluctuation $\Delta T \equiv \ell^2 C_{Tg} T_{\text{CMB}} / (2\pi)$. We then have

$$\Delta T = -0.167 \mu\text{k} \times \frac{\pi}{\ell} \int_{z_1}^{z_2} \Delta_{eg}^2 \left(\frac{\ell}{\chi_e}, z_e \right) \left[\frac{v_{\text{eff}}(\hat{n}_e, z_e)}{10 \text{km/s}} \right] (1 + z_e)^2 \chi_e \bar{n}_g(z_e) dz_e. \quad (3.16)$$

Notice that \bar{n}_g is normalized such that $\int_{z_1}^{z_2} \bar{n}_g(z) dz = 1$. The cross correlation depends on not only the bubble collision parameters, but also on the galaxy redshift and galaxy bias. For brevity, we only show the result for case B with $\theta_e = 0$ and $B = 10^{-3}$, for five redshift bins of [0.01, 0.3], [0.9, 1.1], [1.9, 2.1], [2.9, 3.1] & [3.9, 4.1] (Fig. 13). Results for other values of B scale with $B/10^{-3}$. We adopt a simple linear bias for galaxy overdensity, $\delta_g = b_g \delta_m$ and adopt $b_g = 1$ unless otherwise specified. ΔT defined here is not only proportional to the kSZ signal in the given redshift range, but also proportional to the density fluctuation in the given redshift range. Hence, comparing ΔT over different redshifts can be misleading. It is better to interpret this as the kSZ signal weighted by the r.m.s fluctuation of galaxies in the given redshift bin.

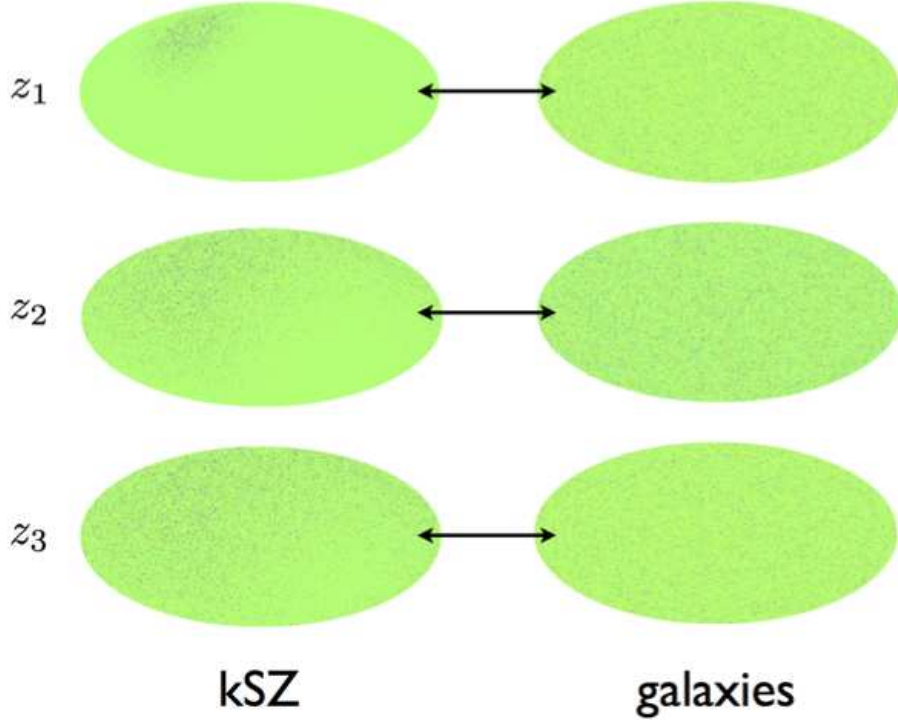


Figure 12. A schematic of the correlation between kSZ and the distribution of galaxies. In each redshift bin (vertical), the kSZ effect maps the density of free electrons $\delta_e(\theta, \phi, z_e)$ contained in galaxies (right panel) to CMB temperature (left panel), with a varying amplitude determined by the collision-induced velocity field $v_{\text{eff}}(\theta, \phi, z_e)$ (e.g. as shown in Figs. 3-6). The measured kSZ effect in CMB alone would be a sum over all redshift bins, however the kSZ-galaxy correlation allows one to reconstruct the velocity field as a function of redshift; this is kSZ tomography.

4 Using kSZ tomography to search for bubble collisions

The kSZ-galaxy cross correlation has unique directional dependence, due to the directional dependence in v_{eff} . This characteristic directional dependence is the key to isolating the weak kSZ effect induced by a bubble collision from overwhelming contaminations such as primary CMB and cosmic infrared background. This section focuses on understanding this directional dependence (§4.1), and utilizing the directional dependence to search for bubble collisions (§4.2).

4.1 The directional dependence of kSZ-galaxy cross correlation

To detect a characteristic directional dependence of the kSZ-galaxy cross correlation, in observations we can split the survey sky into patches of a few degrees in size. The measured cross power spectrum depends not only on the multipole ℓ , but also the relative direction between the patch center and the bubble collision center. We denote $C_i(\ell)$ as the measured cross power spectrum in the i -th patch centered on \hat{n}_i . For redshift bins of size $\Delta z \sim 0.2$, $v_{\text{eff}}(\hat{n}, z)$ does not vary significantly over the patch and over the redshift range. We can therefore write $C_i(\ell)$ as a spatially modulated power

$$C_i(\ell) = C_{\text{pivot}}(\ell|\hat{n}_{\text{pivot}})f(\hat{n}_i) . \quad (4.1)$$

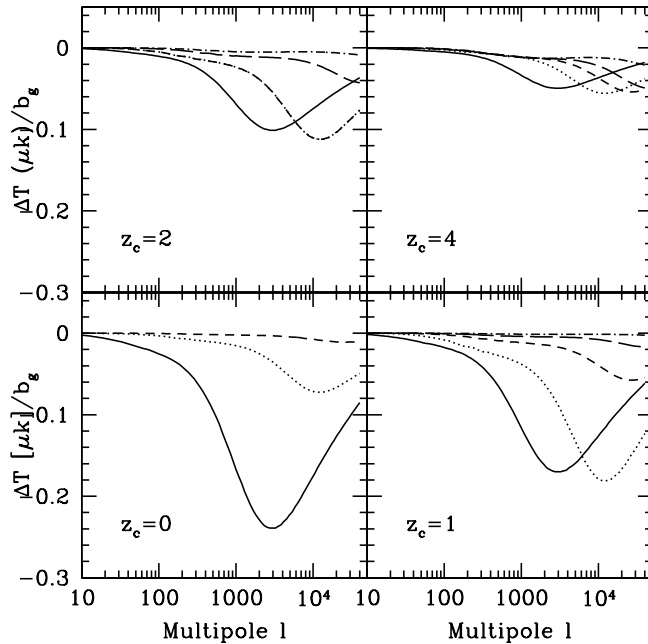


Figure 13. The kSZ-galaxy cross power spectra for $B = 10^{-3}$ toward the center of bubble collision ($\theta_e = 0^\circ$). Solid, dot, short dash, long dash and dot-dash curves have galaxies in the range $[0.01, 0.3]$, $[0.9, 1.1]$, $[1.9, 2.1]$, $[2.9, 3.1]$, $[3.9, 4.1]$, respectively.

where we have chosen to normalize the power against a pivot direction \hat{n}_{pivot} , nominally chosen to be the collision centre. Since the velocity as a function of direction does not vary strongly in a degree-size patch, we can neglect the ℓ dependence in f that comes with the small angular scale variation of the velocity. From Eq. 3.15, we can then approximate f as

$$f_i \equiv f(\hat{n}_i) \simeq \frac{\int_{z_1}^{z_2} dz \bar{n}_e a \bar{n}_g \chi v_{\text{eff}}(\hat{n}_i, z)}{\int_{z_1}^{z_2} dz \bar{n}_e a \bar{n}_g \chi v_{\text{eff}}(\hat{n}_{\text{pivot}}, z)}. \quad (4.2)$$

In Fig. 14 we show f computed from the definition Eq. 4.1; as can be seen in this figure, neglecting the ℓ dependence in f is an excellent approximation. Furthermore, it shows that Eq. 4.2 excellently describes the directional dependence. Therefore, given the parameters A , B , \hat{n}_c and x_c , we can predict the variation of cross power from one patch to another, with no need of detailed modelling of electron-galaxy cross correlation. In particular we have $f(\theta_e = \pi/2) = 0$, due to the azimuthal symmetry. Later on we will use Eq. 4.2 for designing optimal weighting to boost the cross-correlation signal.

4.2 The optimal weighting for bubble collisions

For a fixed redshift bin, we combine all available patches on the sky to obtain a linearly weighted cross correlation

$$C^W(\ell) = \sum_i C_i^{\text{obs}}(\ell) W_i. \quad (4.3)$$

Here the measured cross power spectrum is $C_i^{\text{obs}} = C_i + N_i$ where N_i is the sum of both statistical and systematic noise. The optimal weighting depends on the priors we place on

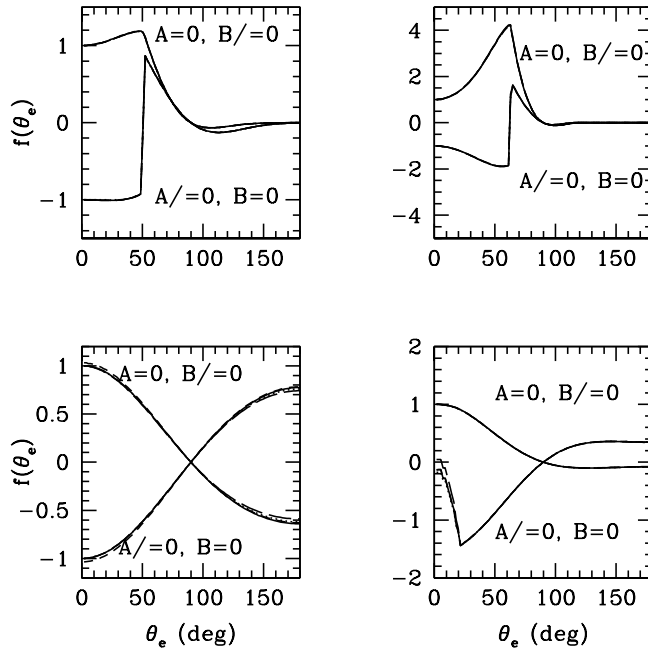


Figure 14. The directional dependence of kSZ-galaxy cross correlation $f(\theta_e|\ell)$. The panels are for $[0.01, 0.3]$ (bottom left), $[0.9, 1.1]$ (bottom right), $[1.9, 2.1]$ (top left) and $[3.9, 4.1]$ (top right). In each panel, there are four curves for $\ell = 1000$ (solid), 3000 (dot), 9000 (short dash) and the approximation Eq. 4.2 (long dash), respectively. All the curves with $A = 0$ and $B \neq 0$ are normalized to unity at $\theta_e = 0^\circ$. For clarity, curves with $A \neq 0$ and $B = 0$ are normalized to -1 at $\theta_e = 0^\circ$. One exception is the redshift bin $[0.9, 1.1]$. It has $\Delta T(\theta_e = 0^\circ) \simeq 0$. So we normalize with the value at $\theta_e = 45^\circ$ instead. Curves of different ℓ overlap over each other and are barely distinguishable against each other. This shows that (1) $f(\theta_e|\ell)$ has negligible ℓ dependence ($f(\theta_e|\ell) \simeq f(\theta_e)$) and (2) the approximation Eq. 4.2 describes $f(\theta_e)$ to excellent accuracy.

the noise term. We discuss two limiting cases. One is the optimistic case that all large scale structure related components (other than kSZ) in the CMB maps have been removed without bias by combining multiple frequency bands. In this limit, the expectation value of N_i is zero ($\langle N_i \rangle = 0$). The r.m.s error of the weighted correlation is

$$\langle N^{W,2} \rangle = \sum_i W_i^2 \sigma_i^2 . \quad (4.4)$$

Here, $\sigma^2 \equiv \langle N_i^2 \rangle$. The normalization of W is irrelevant. However it is convenient to fix it in order to find the optimal weighting. We choose the normalization

$$C^W(\ell) = C_{\text{pivot}}(\ell) \Rightarrow \sum_i W_i f_i = 1 . \quad (4.5)$$

The optimal weighting is then

$$W_i = \frac{f_i / \sigma_i^2}{\sum_j f_j^2 / \sigma_j^2} . \quad (4.6)$$

The second case is more conservative, and perhaps more realistic. In this case, there are residual large scale structure related components other than kSZ in the CMB maps. Therefore

$\langle N_i \rangle \neq 0$. With a modest prior that these systematic contaminants are statistically isotropic, we need $\sum_i W_i = 0$ to eliminate these contaminants in the cross correlation. The optimal unbiased weighting must minimize

$$\sum_i W_i^2 \sigma_i^2 - \lambda_1 \left(\sum_i W_i f_i - 1 \right) - \lambda_2 \sum_i W_i \quad (4.7)$$

Here, $\sigma_i^2 \equiv \langle N_i^2 \rangle - \langle N_i \rangle^2$. $\lambda_{1,2}$ are the two Lagrangian multipliers for the constraints $\sum_i W_i f_i = 1$ and $\sum_i W_i = 0$ respectively. The solution is

$$W_i = \frac{[f_i - \langle f \rangle_S] / \sigma_i^2}{[\langle f^2 \rangle_S - \langle f \rangle_S^2] \sum_i 1 / \sigma_i^2} . \quad (4.8)$$

$\langle f \rangle_S$ is the average over the survey area with the weighting as follows,

$$\langle f \rangle_S = \frac{\sum_i f_i / \sigma_i^2}{\sum_i 1 / \sigma_i^2} . \quad (4.9)$$

The optimal weighting derived earlier for the case of dark flow [67, 69] is a special case corresponding to identical noise of different patches. The weighted noise is

$$\langle N^{W,2} \rangle = \frac{1}{\langle f^2 \rangle_S - \langle f \rangle_S^2} \times \frac{1}{\sum_i 1 / \sigma_i^2} . \quad (4.10)$$

The ratio of two weighted noises (case one versus case two) is $1 - \langle f \rangle_S^2 / \langle f^2 \rangle_S \leq 1$. This inequality confirms our expectation that case two is more conservative and hence has larger error.

To be conservative, we will consider the second case in our forecast. The total signal to noise combining measurements at all ℓ in a given redshift bin is

$$\left[\frac{S}{N} \right]_{\text{tot},z}^2 = \sum_{\ell} C_{\text{pivot}}^2(\ell) [\langle f^2 \rangle_S - \langle f \rangle_S^2] \left[\sum_i 1 / \sigma_i^2(\ell) \right] . \quad (4.11)$$

This assumes that errors in different ℓ bins are uncorrelated. Finally we need to combine measurements for all redshift bins to obtain the final forecast for signal to noise

$$\left[\frac{S}{N} \right]_{\text{tot}}^2 = \sum_z \left[\frac{S}{N} \right]_{\text{tot},z}^2 . \quad (4.12)$$

We adopt the Gaussian approximation to evaluate σ_i ,

$$\begin{aligned} \sigma_i^2 &= \frac{C_{Tg,i}^2 + (C^{\text{CMB}} + C_i^N B^{-2} + C^{\text{kSZ}} + C_i^{\text{For}})(C_g + C_g^N)}{2\ell\Delta\ell f_{\text{sky},i}} \\ &\simeq \frac{(C^{\text{CMB}} + C_i^N B^{-2} + C^{\text{kSZ}} + C_i^{\text{For}})(C_g + C_g^N)}{2\ell\Delta\ell f_{\text{sky},i}} . \end{aligned} \quad (4.13)$$

Here, $B = B(\ell)$ is the beam of CMB experiment. C_i^N is the instrument noise power spectrum at the i -th patch of the sky. Due to variation in the exposure, C^N varies across the sky. C^{kSZ} is the power spectrum of the total kSZ effect whose major contribution is the conventional

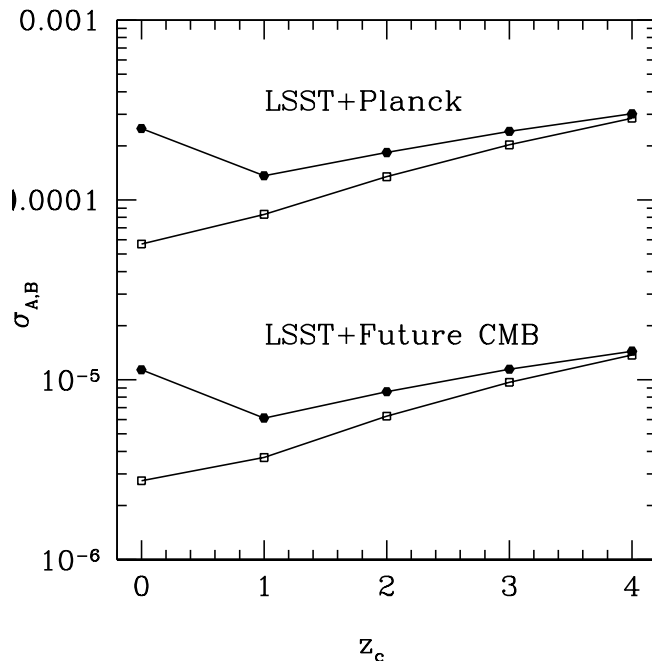


Figure 15. The forecasted constrain on bubble collision. For the future CMB experiment, we adopt a FWHM= $2'$ and a noise level of $1\mu\text{K}$ per square arcminute. The overlapping sky area is taken as $f_{\text{sky}} = 0.5$. Points with filled circles are for the case of $A \neq 0$ and $B = 0$. Points with open square are for the case of $A = 0$ and $B \neq 0$. For the angular resolution of Planck, primary CMB overwhelms. So Planck in combination with LSST has limited capability to detect the kSZ generated by bubble collision. A future CMB experiment with better resolution can improve the measurement by orders of magnitude. We estimate that a PRISM-like experiment has the capability of measure A and B with r.m.s error of 10^{-5} . Constraints on B are systematically better than constraints on A when $z_c \leq 4$, simply reflecting the fact that when $A = B$, the case B has on the average larger curvature potential inside of our horizon. The two constraints at $z_c = 4$ are roughly the same, for the reason that they have roughly the same mean curvature perturbation inside of our horizon.

kSZ effect including patchy reionization. C^{For} is the power spectrum of residual foregrounds, which includes all large scale structure related contaminants such as CIB, the relativistic thermal SZ effect and the cosmic radio background. Since this relies heavily on multi frequency information, whose effectiveness depends on exposure time, this may also vary with direction. Variation of the gray-body power index and the temperature of CIB over the sky can add more directional variation. Given uncertainties in the modelling of the conventional kSZ effect and foregrounds, we will adopt a flat spectrum $\ell^2(C^{\text{kSZ}} + C^{\text{For}})/(2\pi)(2.73\text{K})^2 = 10\mu\text{K}^2$. C_g is the galaxy auto power spectrum in the given patch of the sky and the given redshift bin. C_g^N is the associated (statistical) noise. We only consider shot noise so that $C_g^N = 4\pi f_{\text{sky},i}/N_{g,i}$. $f_{\text{sky},i}$ is the fractional sky coverage. $N_{g,i}$ is the total number of galaxies in this patch of the sky in the given redshift bin. The last approximation of Eq. 4.13 holds since the kSZ effect induced by bubble collision is always subdominant/negligible to sum of other CMB components/contaminations.

Given that the bubble collision induced kSZ signal is weak, we require both advanced CMB experiments and galaxy surveys in order to be sensitive to bubble collisions. Fig. 15

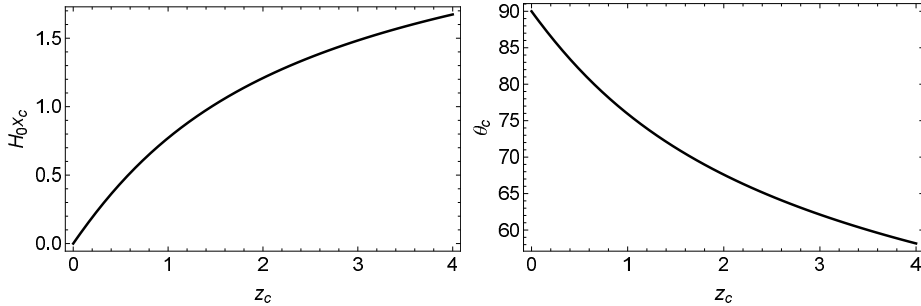


Figure 16. The relation between x_c and z_c (left) and θ_c and z_c (right) in Λ CDM over the range in redshifts in Fig. 15. x_c is the x-coordinate of the location of the causal boundary and z_c is the corresponding redshift ($x_c = \chi(z_c)$). θ_c is the angular radius of the bubble collision on the primary CMB sky ($\cos \theta_c = x_c / \chi_{\text{dec}}$).

shows the forecasted constraints on A (B), for the combination of Planck and LSST [88]. For LSST, we adopt $\bar{n}_g = 30/\text{arcmin}^2$. The redshift distribution is adopted as $n_g(z) \propto z^2 \exp(-z/z_*)$ and $z_* = 0.5$. We assume that LSST and Planck overlap over 50% of the sky. This combination has the capability of detecting the bubble collision if $\max[A, B] \gtrsim 10^{-4}$. Planck has a limited angular resolution of $\sim 10'$ ($\ell \gtrsim 2000$), so it misses the majority of the kSZ signal generated by the bubble collision, which peaks at $\ell \sim 10^4$. To capture the majority of it, the angular resolution of CMB experiment should be improved to $\sim 2'$. Therefore we consider a PRISM-like CMB experiment [89] with FWHM=2' and a low noise level of $1\mu\text{K}^2$ per arcmin^2 . Combined with the LSST survey, the constraint on A and B can be improved by one order of magnitude to $\sigma_{A/B} \gtrsim 10^{-5}$.

Two major uncertainties in this forecast, besides the bubble collision parameters, are the level of residual foreground contamination and the level of non-Gaussianity of residual foreground near the angular resolution limit. The first can be alleviated by cleaner foreground removal with more frequency bands and lower instrumental noise. A lower residual foreground will make the measurement more noise dominated at small scales, and therefore alleviate uncertainties caused by non-Gaussianities of residual foreground.

4.3 Comparison with constraints from the primary CMB

We can compare this sensitivity to what has been achieved using CMB temperature [48, 51] and what has been forecast for CMB temperature and polarization [23]. These works all analyzed only the linear template, so only provide constraints and projections for the amplitude A . CMB studies work with the angular radius of the collision on the CMB sky, given by

$$\cos \theta_c = \frac{x_c}{\chi_{\text{dec}}} . \quad (4.14)$$

where x_c is the comoving position of the causal boundary and $\chi_{\text{dec}} \simeq 3H_0^{-1}$ is the comoving distance to the surface of last scattering. To assist in comparison between observables in Fig. 16 we show the relation between x_c , z_c , and θ_c for the Planck best-fit Λ CDM cosmology.

The sensitivity of the hierarchical Bayesian method of Ref. [48] is given by the 50% completeness curve for the detection of candidate bubble collisions (Figure 5 of Ref. [48]). The constraint is expressed in terms of z_0 , the central amplitude of the collision in the CMB temperature. In the Sachs-Wolfe approximation, this is one third of the primordial

Newtonian potential Ψ_i , and in the notation of Ref. [48] we can identify $A \simeq 3z_0$. Over the range of θ_c relevant for Fig. 15, the completeness curve is fairly flat, and we obtain a sensitivity of $|A| \sim 1.5 \times 10^{-4}$. The analysis of candidate features in WMAP7 data failed to provide evidence for bubble collisions, we can interpret this sensitivity as a constraint.

Ref. [51] performed an analysis of the WMAP7 data using different methods, obtaining the constraint $-2.10 \times 10^{-4} < aH_0^{-1}(\sin \theta_c)^{4/3} < 2.13 \times 10^{-4}$ where a is the amplitude of the linear template in the comoving gauge. On super horizon scales, we can relate this to A in the Newtonian gauge by a factor of 3/5. We then obtain a constraint on the amplitude A of $|A| < 1.2(\sin \theta_c)^{-4/3} \times 10^{-4}$. The angular dependence is not important over the range of θ_c probed by kSZ tomography, so we can express the constraint as $|A| < 1.2 \times 10^{-4}$, in agreement with Ref. [48].

Extra information is carried by CMB polarization [23]. Collisions on the angular scales probed by kSZ tomography could be detected at similar signal to noise in CMB polarization as in CMB temperature. The cosmic-variance limited CMB signal to noise using both temperature and polarization will therefore be close to the constraints quoted above.

4.4 Constraints on the lagrangian underlying eternal inflation

Auxiliary information is needed to interpret our constraints as constraints on fundamental parameters in the scalar field lagrangian underlying eternal inflation, as outlined in Sec. 2. The most important auxiliary observables are the energy density in curvature Ω_k^{obs} and the scalar to tensor ratio r^{obs} . The fundamental limit on observing curvature is $\Omega_k \sim 10^{-5}$, when it becomes indistinguishable from a long-wavelength curvature perturbation. A next-generation CMB polarization experiment can in principle reach sensitivities for the scalar to tensor ratio of $r \sim 10^{-3}$ [90], while futuristic space-based gravitational wave detectors may probe down to $r \sim 10^{-6}$ [91].

The first case to consider is that of collisions between identical bubbles, in which case we can identify $B = 2\Omega_k^{\text{obs}}(1 - \cos \Delta x_{\text{sep}})^2 / 15$. In this scenario, kSZ tomography can probe the entire observable range of Ω_k^{obs} . If curvature is detected in the future, kSZ tomography can completely rule out the presence of identical bubble collisions in our observable universe.

For collisions between non-identical bubbles, the story is not as clear-cut. Generally speaking, we can only constrain combinations of the fundamental parameters

$$\frac{\delta\phi_0^{\text{coll}}}{M_{\text{pl}}} (1 - \cos \Delta x_{\text{sep}}) < \frac{5}{2} \sqrt{\frac{r_{\text{obs}}}{8\Omega_k^{\text{obs}}}} A_{\text{limit}} \quad (4.15)$$

$$\sqrt{r_{\text{coll}}} \frac{H_I^{\text{coll}}}{H_I^{\text{obs}}} (1 - \cos \Delta x_{\text{sep}})^2 < \frac{15}{2} \frac{\sqrt{r_{\text{obs}}}}{\Omega_k^{\text{obs}}} B_{\text{limit}} \quad (4.16)$$

where A_{limit} and B_{limit} are limits on these amplitudes obtained through kSZ tomography (or another method). The first constraint involving $\delta\phi_0^{\text{coll}}$ depends on the ratio of r_{obs} and Ω_k^{obs} , both of which could be unobservably small. Smaller values of r_{obs} correspond to small-field models of inflation, which arguably need more tuning to get a large number of e -folds, and therefore one might not expect an arbitrarily small Ω_k^{obs} . This is the only theoretical guidance the authors imagine that one might obtain in the absence of a more fundamental understanding of inflation. However, in the optimistic scenario where both curvature and tensors are detected, meaningful limits on fundamental parameters can be set using kSZ tomography.

5 Discussion and Summary

In this paper we have examined how collisions between bubble universes, a possible relic of eternal inflation, might be observed using the kinetic Sunaev Zel’dovich effect. The kSZ effect we consider is a census of the CMB dipole observed by free electrons on our past light cone, which inhabit nearly every vantage point in our observable universe. Because the kSZ effect is a census, it has the power to probe large-scale inhomogeneities far better than the cosmic variance limited results associated with observations made from one position. Unfortunately, being a secondary effect, the amplitude of the kSZ signature expected in the CMB is tiny, of order $1\mu\text{K}$. However, a crucial observation is that free electrons trace large scale structure, giving rise to a strong correlation between the kSZ effect and large scale structure in the universe. This redshift-dependent cross-correlation, known as kSZ tomography, can be used as a sensitive probe of ultra-large scale inhomogeneities.

The effects of a bubble collision are encoded in a planar-symmetric curvature perturbation, and for the class of observers in the vicinity of the causal boundary of the collision, can be described by three constants [25, 29]: the position of the causal boundary (comoving position x_c or equivalently the redshift z_c), the amplitude of a linear potential perturbation (A), and the amplitude of a quadratic potential perturbation (B). The angular dependence of the kSZ effect produced by bubble collisions depends on the parameters A, B , and z_c . This makes the kSZ effect a powerful discriminator between models, and is essential for isolating the kSZ signature from contaminants.

The main result of our analysis are summarized in Fig. 15. We forecast that Planck and LSST can put useful constraints $\sigma_{A/B} \sim 10^{-4}$ on the bubble collision parameters A and B over the allowed range of z_c . The primary source of this limit come from the angular resolution and instrumental noise of Planck. For LSST and a next-generation CMB experiment such as PRISM, the sensitivity can be improved by roughly an order of magnitude to $\sigma_{A/B} \sim 10^{-5}$. The in-principle limit on sensitivity, in the absence of instrumental noise and assuming perfect foreground subtraction, can be estimated as roughly $\sigma_{A/B} \sim 10^{-10}$.⁷ Nearly cosmic variance limited constraints exist for A from the primary CMB [46–49], yielding $A \lesssim 10^{-4}$. Therefore, kSZ can in principle beat the cosmic-variance limited constraints from the primary CMB by nearly 6 orders of magnitude. To put this in perspective, using e.g. $A \sim \sqrt{\Omega_k^{\text{obs}}} \sim e^{-N_{\text{extra}}}$, where N_{extra} is the number of extra e -folds beyond the number necessary to solve the horizon problem, it would be possible at this sensitivity to probe the initial conditions for inflation up to 23 e -folds beyond what is necessary to solve the horizon problem.

To connect the constraints on A and B to constraints on the fundamental parameters in the scalar field lagrangian underlying eternal inflation, ancillary data is needed. In particular, a detection of curvature and primordial tensor modes would allow for a direct constraint on

⁷This number is obtained with several approximations and can only be treated as an order of magnitude estimation. (1) We neglect primary CMB. This is indeed valid at $\ell \gtrsim 4000$ where other components dominate. (2) we assume perfect foreground removal and vanishing instrument noise. (3) we assume sufficiently high galaxy number density such that $C_g^N \ll C_g$. Therefore we can neglect all terms except C^{kSZ} and C'_g in Eq. 4.13. (4) we assume a perfect cross correlation between the kSZ effect in a given redshift bin and the galaxy overdensity in that redshift bin, namely the cross correlation coefficient $r = 1$. These approximations allow us to sum over all ℓ and z bins and obtain $(S/N)_{\text{tot}}^2 \sim \ell_{\text{max}}^2 f_{\text{sky}} C_{\text{bubble}}^{\text{kSZ}} / C^{\text{kSZ}}$. We first consider case B. Using $\ell^2 C_{\text{bubble}}^{\text{kSZ}} / (2\pi) \sim B \times 10^2 \mu\text{K}$ (Fig. 9) and $\ell^2 C^{\text{kSZ}} / (2\pi) \sim 1\mu\text{K}$ for all ℓ , we obtain $(S/N)_{\text{tot}}^2 \sim 10^{10} B (\ell_{\text{max}}/10^4)^2 f_{\text{sky}}$, valid for $|B| \ll 1$. For $\ell_{\text{max}} = 10^4$, we obtain a sensitivity of $\sigma_B \sim 10^{-10}$. Constraint on A is of the same order of magnitude. The reason is that the kSZ power spectrum for case A is comparable to case B when $A = B$ (Fig. 10 versus Fig. 11), and it scales linearly with A . Nevertheless, constraint on A can be a factor of ~ 2 weaker than B due to a factor of ~ 2 weaker signal (Fig. 10 versus Fig. 11).

the width of the potential barrier describing the collision bubble and the relative energy scale of inflation inside the collision and observation bubbles. In the most constraining scenario ($\Omega_k^{\text{obs}} \sim 10^{-2}$, $r_{\text{obs}} \sim 10^{-6}$), the in-principle sensitivity of the kSZ effect would allow for constraints on the properties of the collision bubble down to scales of order $10\text{-}10^3$ TeV ($\delta\phi_0^{\text{coll}} < 10^3$ TeV, $\sqrt{r_{\text{coll}}}H_I^{\text{coll}} < H_I^{\text{obs}}10^{-10} < 10$ TeV). These scales are potentially relevant for supersymmetric or grand unified theories which give rise to eternal inflation.

Bubble collisions in eternal inflation are a predictive theory of inhomogeneous initial conditions for our Universe. In this respect, they provide a testbed for addressing more generally what we might learn about the observability of inflationary initial conditions by providing a benchmark model. Clearly, kSZ tomography has enormous potential to probe the initial conditions for inflation.

Acknowledgment.—PJZ was supported by the National Science Foundation of China (Grant No. 11025316, 11320101002, 11433001), National Basic Research Program of China (973 Program 2015CB857001), the Strategic Priority Research Program "The Emergence of Cosmological Structures" of the Chinese Academy of Sciences (Grant No. XDB09000000), the NAOC-Templeton beyond the horizon program, and the key laboratory grant from the Office of Science and Technology, Shanghai Municipal Government (No. 11DZ2260700). Research at Perimeter Institute is supported by the Government of Canada through Industry Canada and by the Province of Ontario through the Ministry of Research and Innovation. MCJ is supported by the National Science and Engineering Research Council through a Discovery grant. PJZ and MCJ thank the support of National Science Foundation Grant No. PHYS-1066293, the Simons foundation, and the hospitality of the Aspen Center for Physics where this work was initiated.

A Linear Evolution of gravitational potential and velocity

The bubble collision generated perturbation is a mixture of both superhorizon and subhorizon modes. Therefore the exact evolution of Ψ and v has to be solved numerically. We adopt the conformal Newtonian gauge and solve the following equations for radiation and cold dark matter in a flat universe [92],

$$\begin{aligned}
\frac{d\Theta_{r,0}}{dx} &= -\frac{k}{aH}\Theta_{r,1} - \frac{d\Psi}{dx} , \\
\frac{d\Theta_{r,1}}{dx} &= \frac{k}{3aH}\Theta_{r,0} - \frac{k}{3aH}\Psi , \\
\frac{d\delta}{dx} &= -i\frac{k}{aH}v - 3\frac{d\Psi}{dx} , \\
\frac{dv}{dx} &= -v + i\frac{k}{aH}\Psi , \\
\frac{d\Psi}{dx} &= \frac{1}{2}\frac{H_0^2}{H^2}(\Omega_m a^{-3}\delta + 4\Omega_r a^{-4}\Theta_{r,0}) - \Psi - \frac{k^2}{3a^2 H^2}\Psi .
\end{aligned}
\tag{A.1}$$

We have changed the argument from the conformal time τ to $x = \ln a$. We numerically solve the above five equations for the variables $(\Theta_{r,0}, \Theta_{r,1}, \delta, -iv, \Psi)$ using a modified version of the CMBFAST package [93]. The adiabatic initial condition is

$$\Theta_{r,0} = \frac{1}{2}\Psi_i, \delta = \frac{3}{2}\Psi_i, \Theta_{r,1} = 0, v = 0 .
\tag{A.2}$$

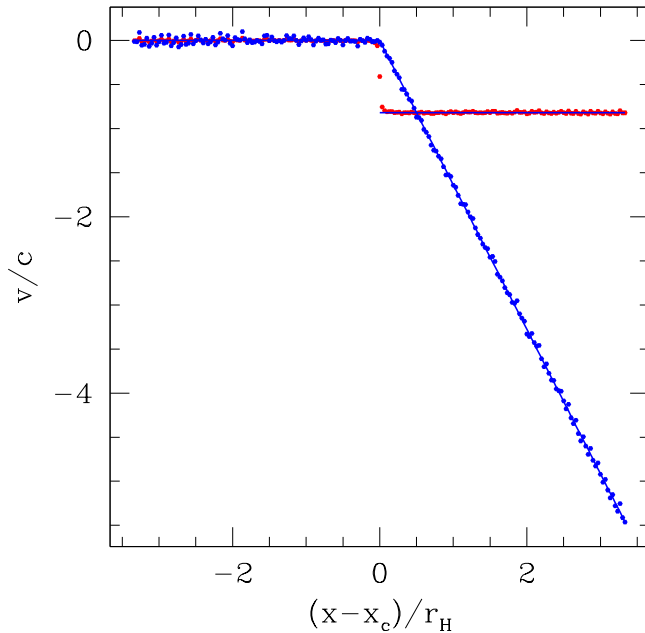


Figure 17. The velocity field at $z = 0$, for case A and case B. The data points are the numerically evaluated velocity field and the solid lines are the analytical prediction assuming superhorizon evolution. The two agree excellently. Hence we will adopt the superhorizon evolution throughout the paper, which allow us to address many calculations analytically.

We find that, although there are subhorizon modes in the initial perturbation, the overall evolution of Φ and v are excellently described by the superhorizon evolution (Fig. 17). For superhorizon modes, the evolution in potential at early time where the cosmological constant is negligible is [79, 92]

$$\Psi_{\text{SH}}(a) = \Psi_{\text{SH},i} \frac{16\sqrt{1+y} + 9y^3 + 2y^2 - 8y - 16}{10y^3}. \quad (\text{A.3})$$

Here, $y \equiv a/a_{\text{eq}}$ and $a_{\text{eq}} = \Omega_R/\Omega_m$ is the scale factor at the epoch of the radiation-matter equality. When $y \gg 1$, $\Psi_{\text{SH}} \rightarrow \Psi_{\text{SH},i}9/10$. On the other hand, the evolution of gravitational potential at late time where radiation is negligible is

$$\Psi(a) \propto \frac{5}{2}\Omega_m \frac{E(a)}{a} \int_0^a \frac{da'}{E^3(a')a'^3}. \quad (\text{A.4})$$

Here $E(a) = \sqrt{\Omega_m a^{-3} + \Omega_\Lambda}$ is the normalized Hubble parameter and by setting $\Omega_R = 0$. This result holds for both the subhorizon and superhorizon modes [94]. The integral above can be excellently fitted by [95]

$$g(a) \equiv \frac{5\Omega_m(a)/2}{\Omega_m^{4/7}(a) - \Omega_\Lambda(a) + (1 + \frac{\Omega_m(a)}{2})(1 + \frac{\Omega_\Lambda(a)}{70})}. \quad (\text{A.5})$$

Hence the evolution of a superhorizon mode over all cosmic epoch can be well approximated by

$$D_{\Psi}(a) \equiv \frac{\Psi_{\text{SH}}(a)}{\Psi_{\text{SH},i}} = \frac{16\sqrt{1+y} + 9y^3 + 2y^2 - 8y - 16}{10y^3} \left[\frac{5}{2}\Omega_m \frac{E(a)}{a} \int_0^a \frac{da'}{E^3(a)a^3} \right] \quad (\text{A.6})$$

$$\simeq \frac{16\sqrt{1+y} + 9y^3 + 2y^2 - 8y - 16}{10y^3} \times g(a) .$$

On the other hand, we have [79]

$$\mathbf{v} = -\frac{2a^2 c^2 H(a)}{H_0^2 \Omega_m} \frac{y}{4+3y} \left[\nabla \Psi + \frac{d\nabla \Psi}{d \ln a} \right] = -\frac{2a^2 c^2 H(a)}{H_0^2 \Omega_m} \frac{y}{4+3y} \left[D_{\Psi} + \frac{dD_{\Psi}}{d \ln a} \right] \nabla \Psi_i . \quad (\text{A.7})$$

We define the velocity growth rate function as

$$D_v(a) \equiv \frac{2a^2 H(a)}{H_0^2 \Omega_m} \frac{y}{4+3y} \left[D_{\Psi} + \frac{dD_{\Psi}}{d \ln a} \right] . \quad (\text{A.8})$$

D_v and D_{Ψ} are related by

$$D_v = \frac{1}{a} \int_0^a \frac{D_{\Psi}(a)}{aH} da . \quad (\text{A.9})$$

We find that Eq. A.6 and A.7 describe the evolution of the given gravitational potential (Eq. 2.2) and the induced velocity excellently (Fig. 17). Numerically we find that subhorizon modes slightly smooth the potential and velocity near the causal boundary. But these modes are negligible for the purpose of this paper. Therefore we will adopt the above analytical results for superhorizon modes to follow the evolution of bubble collision generated perturbation.

References

- [1] L. Susskind, *The anthropic landscape of string theory*, [hep-th/0302219](#).
- [2] S. R. Coleman, *The Fate of the False Vacuum. 1. Semiclassical Theory*, *Phys. Rev.* **D15** (1977) 2929–2936.
- [3] J. Callan, Curtis G. and S. R. Coleman, *The fate of the false vacuum. 2. first quantum corrections*, *Phys. Rev.* **D16** (1977) 1762–1768.
- [4] S. R. Coleman and F. De Luccia, *Gravitational Effects on and of Vacuum Decay*, *Phys. Rev.* **D21** (1980) 3305.
- [5] J. R. Gott, *Creation of open universes from de sitter space*, *Nature* **295** (1982) 304–307.
- [6] J. R. Gott and T. S. Statler, *Constraints on the formation of bubble universes*, *Phys. Lett.* **B136** (1984) 157–161.
- [7] M. Bucher, A. S. Goldhaber, and N. Turok, *An open universe from inflation*, *Phys. Rev.* **D52** (1995) 3314–3337, [[hep-ph/9411206](#)].
- [8] J. Garriga, A. H. Guth, and A. Vilenkin, *Eternal inflation, bubble collisions, and the persistence of memory*, *Phys. Rev.* **D76** (2007) 123512, [[hep-th/0612242](#)].
- [9] A. Aguirre, M. C. Johnson, and A. Shomer, *Towards observable signatures of other bubble universes*, *Phys. Rev.* **D76** (2007) 063509.

- [10] S. W. Hawking and I. G. Moss, *Supercooled Phase Transitions in the Very Early Universe*, *Phys. Lett.* **B110** (1982) 35.
- [11] S. W. Hawking, I. G. Moss, and J. M. Stewart, *Bubble Collisions in the Very Early Universe*, *Phys. Rev.* **D26** (1982) 2681.
- [12] Z.-C. Wu, *Gravitational effects in bubble collisions*, *Phys. Rev.* **D28** (1983) 1898–1906.
- [13] I. G. Moss, *Black hole formation from colliding bubbles*, [gr-qc/9405045](#).
- [14] A. Aguirre and M. C. Johnson, *Towards observable signatures of other bubble universes II: Exact solutions for thin-wall bubble collisions*, *Phys. Rev.* **D77** (2008) 123536.
- [15] A. Aguirre, M. C. Johnson, and M. Tysanner, *Surviving the crash: assessing the aftermath of cosmic bubble collisions*, *Phys.Rev.* **D79** (2009) 123514, [[arXiv:0811.0866](#)].
- [16] A. Aguirre and M. C. Johnson, *A Status report on the observability of cosmic bubble collisions*, *Rept.Prog.Phys.* **74** (2011) 074901, [[arXiv:0908.4105](#)].
- [17] J. Kozaczuk and A. Aguirre, *Multiple Cosmic Collisions and the Microwave Background Power Spectrum*, [arXiv:1206.5038](#).
- [18] S. Chang, M. Kleban, and T. S. Levi, *Watching Worlds Collide: Effects on the CMB from Cosmological Bubble Collisions*, *JCAP* **0904** (2009) 025, [[arXiv:0810.5128](#)].
- [19] S. Chang, M. Kleban, and T. S. Levi, *When worlds collide*, *JCAP* **0804** (2008) 034, [[arXiv:0712.2261](#)].
- [20] B. Czech, M. Kleban, K. Larjo, T. S. Levi, and K. Sigurdson, *Polarizing Bubble Collisions*, *JCAP* **1012** (2010) 023, [[arXiv:1006.0832](#)].
- [21] B. Freivogel, M. Kleban, A. Nicolis, and K. Sigurdson, *Eternal Inflation, Bubble Collisions, and the Disintegration of the Persistence of Memory*, *JCAP* **0908** (2009) 036.
- [22] R. Gobetti and M. Kleban, *Analyzing Cosmic Bubble Collisions*, *JCAP* **1205** (2012) 025, [[arXiv:1201.6380](#)].
- [23] M. Kleban, T. S. Levi, and K. Sigurdson, *Observing the Multiverse with Cosmic Wakes*, [arXiv:1109.3473](#).
- [24] M. Kleban, *Cosmic Bubble Collisions*, *Class.Quant.Grav.* **28** (2011) 204008, [[arXiv:1107.2593](#)].
- [25] C. L. Wainwright, M. C. Johnson, H. V. Peiris, A. Aguirre, L. Lehner, et al., *Simulating the universe(s): from cosmic bubble collisions to cosmological observables with numerical relativity*, *JCAP* **1403** (2014) 030, [[arXiv:1312.1357](#)].
- [26] M. C. Johnson and I.-S. Yang, *Escaping the crunch: Gravitational effects in classical transitions*, *Phys.Rev.* **D82** (2010) 065023, [[arXiv:1005.3506](#)].
- [27] M. C. Johnson, H. V. Peiris, and L. Lehner, *Determining the outcome of cosmic bubble collisions in full General Relativity*, *Phys.Rev.* **D85** (2012) 083516, [[arXiv:1112.4487](#)].
- [28] B. Freivogel, G. T. Horowitz, and S. Shenker, *Colliding with a crunching bubble*, [hep-th/0703146](#).
- [29] C. L. Wainwright, M. C. Johnson, A. Aguirre, and H. V. Peiris, *Simulating the universe(s) II: phenomenology of cosmic bubble collisions in full General Relativity*, *JCAP* **1410** (2014), no. 10 024, [[arXiv:1407.2950](#)].
- [30] M. P. Salem, P. Saraswat, and E. Shaghoulian, *Gravity waves from cosmic bubble collisions*, *JCAP* **1302** (2013) 019, [[arXiv:1210.4165](#)].
- [31] B. Czech, *A Novel Channel for Vacuum Decay*, *Phys.Lett.* **B713** (2012) 331–334, [[arXiv:1112.1638](#)].

- [32] M. P. Salem, *Bubble collisions and measures of the multiverse*, *JCAP* **1201** (2012) 021, [[arXiv:1108.0040](#)].
- [33] M. P. Salem, *A Signature of anisotropic bubble collisions*, *Phys.Rev.* **D82** (2010) 063530, [[arXiv:1005.5311](#)].
- [34] K. Larjo and T. S. Levi, *Bubble, Bubble, Flow and Hubble: Large Scale Galaxy Flow from Cosmological Bubble Collisions*, *JCAP* **1008** (2010) 034, [[arXiv:0910.4159](#)].
- [35] R. Easther, J. Giblin, John T., L. Hui, and E. A. Lim, *A New Mechanism for Bubble Nucleation: Classical Transitions*, *Phys.Rev.* **D80** (2009) 123519, [[arXiv:0907.3234](#)].
- [36] J. Giblin, John T., L. Hui, E. A. Lim, and I.-S. Yang, *How to Run Through Walls: Dynamics of Bubble and Soliton Collisions*, *Phys.Rev.* **D82** (2010) 045019, [[arXiv:1005.3493](#)].
- [37] P. Ahlqvist, K. Eckerle, and B. Greene, *Kink Collisions in Curved Field Space*, [[arXiv:1411.4631](#)].
- [38] D.-H. Kim, B.-H. Lee, W. Lee, J. Yang, and D.-h. Yeom, *Gravitational waves from cosmic bubble collisions*, [[arXiv:1410.4648](#)].
- [39] P. Ahlqvist, K. Eckerle, and B. Greene, *Bubble Universe Dynamics After Free Passage*, [[arXiv:1310.6069](#)].
- [40] D.-i. Hwang, B.-H. Lee, W. Lee, and D.-h. Yeom, *Bubble collision with gravitation*, *JCAP* **1207** (2012) 003, [[arXiv:1201.6109](#)].
- [41] J. T. Deskins, J. Giblin, John T., and I.-S. Yang, *Classical Transitions for Flux Vacua*, *JHEP* **1210** (2012) 035, [[arXiv:1207.6636](#)].
- [42] M. A. Amin, E. A. Lim, and I.-S. Yang, *A Clash of Kinks: Phase shifts in colliding non-integrable solitons*, [[arXiv:1308.0605](#)].
- [43] M. A. Amin, E. A. Lim, and I.-S. Yang, *A scattering theory of ultra-relativistic solitons*, [[arXiv:1308.0606](#)].
- [44] B. Freivogel, M. Kleban, M. Rodriguez Martinez, and L. Susskind, *Observational consequences of a landscape*, *JHEP* **03** (2006) 039, [[hep-th/0505232](#)].
- [45] I.-S. Yang, *Probability of Slowroll Inflation in the Multiverse*, *Phys.Rev.* **D86** (2012) 103537, [[arXiv:1208.3821](#)].
- [46] S. M. Feeney, M. C. Johnson, D. J. Mortlock, and H. V. Peiris, *First Observational Tests of Eternal Inflation: Analysis Methods and WMAP 7-Year Results*, *Phys. Rev.* **D84** (2011) 043507, [[arXiv:1012.3667](#)].
- [47] S. M. Feeney, M. C. Johnson, D. J. Mortlock, and H. V. Peiris, *First Observational Tests of Eternal Inflation*, *Phys. Rev. Lett.* **107** (2011) 071301, [[arXiv:1012.1995](#)].
- [48] S. M. Feeney, M. C. Johnson, J. D. McEwen, D. J. Mortlock, and H. V. Peiris, *Hierarchical Bayesian Detection Algorithm for Early-Universe Relics in the Cosmic Microwave Background*, *Phys.Rev.* **D88** (2013) 043012, [[arXiv:1210.2725](#)].
- [49] J. D. McEwen, S. M. Feeney, M. C. Johnson, and H. V. Peiris, *Optimal filters for detecting cosmic bubble collisions*, *Phys. Rev.* **D85** (2012) 103502, [[arXiv:1202.2861](#)].
- [50] **WMAP** Collaboration, C. L. Bennett et al., *The Microwave Anisotropy Probe (MAP) Mission*, *Astrophys. J.* **583** (2003) 1–23, [[astro-ph/0301158](#)].
- [51] S. Osborne, L. Senatore, and K. Smith, *Collisions with other Universes: the Optimal Analysis of the WMAP data*, [[arXiv:1305.1964](#)].
- [52] S. Osborne, L. Senatore, and K. Smith, *Optimal analysis of azimuthal features in the CMB*, [[arXiv:1305.1970](#)].

- [53] C. Dvorkin, H. V. Peiris, and W. Hu, *Testable polarization predictions for models of CMB isotropy anomalies*, *Phys.Rev.* **D77** (2008) 063008, [[arXiv:0711.2321](#)].
- [54] M. J. Mortonson, C. Dvorkin, H. V. Peiris, and W. Hu, *CMB polarization features from inflation versus reionization*, *Phys.Rev.* **D79** (2009) 103519, [[arXiv:0903.4920](#)].
- [55] R. A. Sunyaev and I. B. Zeldovich, *The velocity of clusters of galaxies relative to the microwave background - The possibility of its measurement*, *MNRAS* **190** (Feb., 1980) 413–420.
- [56] E. T. Vishniac, *Reionization and small-scale fluctuations in the microwave background*, *ApJ* **322** (Nov., 1987) 597–604.
- [57] M. G. Haehnelt and M. Tegmark, *Using the Kinematic Sunyaev-Zeldovich effect to determine the peculiar velocities of clusters of galaxies*, *MNRAS* **279** (Mar., 1996) 545, [[astro-ph/9507077](#)].
- [58] C.-P. Ma and J. N. Fry, *Nonlinear Kinetic Sunyaev-Zeldovich Effect*, *Physical Review Letters* **88** (May, 2002) 211301, [[astro-ph/0106342](#)].
- [59] P. Zhang, U.-L. Pen, and H. Trac, *Precision era of the kinetic Sunyaev-Zel’dovich effect: simulations, analytical models and observations and the power to constrain reionization*, *MNRAS* **347** (Feb., 2004) 1224–1233, [[astro-ph/](#)].
- [60] P. Zhang, H. A. Feldman, R. Juszkiewicz, and A. Stebbins, *A new method of measuring the cluster peculiar velocity power spectrum*, *MNRAS* **388** (Aug., 2008) 884–888, [[arXiv:0806.4190](#)].
- [61] N. Hand, G. E. Addison, E. Aubourg, N. Battaglia, E. S. Battistelli, D. Bizyaev, J. R. Bond, H. Brewington, J. Brinkmann, B. R. Brown, S. Das, K. S. Dawson, M. J. Devlin, J. Dunkley, R. Dunner, D. J. Eisenstein, J. W. Fowler, M. B. Gralla, A. Hajian, M. Halpern, M. Hilton, A. D. Hincks, R. Hlozek, J. P. Hughes, L. Infante, K. D. Irwin, A. Kosowsky, Y.-T. Lin, E. Malanushenko, V. Malanushenko, T. A. Marriage, D. Marsden, F. Menanteau, K. Moodley, M. D. Niemack, M. R. Nolta, D. Oravetz, L. A. Page, N. Palanque-Delabrouille, K. Pan, E. D. Reese, D. J. Schlegel, D. P. Schneider, N. Sehgal, A. Shelden, J. Sievers, C. Sifón, A. Simmons, S. Snedden, D. N. Spergel, S. T. Staggs, D. S. Swetz, E. R. Switzer, H. Trac, B. A. Weaver, E. J. Wollack, C. Yeche, and C. Zunckel, *Evidence of Galaxy Cluster Motions with the Kinematic Sunyaev-Zel’dovich Effect*, *Physical Review Letters* **109** (July, 2012) 041101, [[arXiv:1203.4219](#)].
- [62] E. M. George, C. L. Reichardt, K. A. Aird, B. A. Benson, L. E. Bleem, J. E. Carlstrom, C. L. Chang, H. Cho, T. M. Crawford, A. T. Crites, T. de Haan, M. A. Dobbs, J. Dudley, N. W. Halverson, N. L. Harrington, G. P. Holder, W. L. Holzapfel, Z. Hou, J. D. Hrubes, R. Keisler, L. Knox, A. T. Lee, E. M. Leitch, M. Lueker, D. Luong-Van, J. J. McMahon, J. Mehl, S. S. Meyer, M. Millea, L. M. Mocanu, J. J. Mohr, T. E. Montroy, S. Padin, T. Plagge, C. Pryke, J. E. Ruhl, K. K. Schaffer, L. Shaw, E. Shirokoff, H. G. Spieler, Z. Staniszewski, A. A. Stark, K. T. Story, A. van Engelen, K. Vanderlinde, J. D. Vieira, R. Williamson, and O. Zahn, *A measurement of secondary cosmic microwave background anisotropies from the 2500-square-degree SPT-SZ survey*, *ArXiv e-prints* (Aug., 2014) [[arXiv:1408.3161](#)].
- [63] X.-D. Xu, B. Wang, P. Zhang, and F. Atrio-Barandela, *The effect of dark matter and dark energy interactions on the peculiar velocity field and the kinetic Sunyaev-Zel’dovich effect*, *JCAP* **12** (Dec., 2013) 1, [[arXiv:1308.1475](#)].
- [64] X.-d. Xu, B. Wang, and P. Zhang, *Testing Tensor-Vector-Scalar Theory with latest cosmological observations*, *ArXiv e-prints* (Dec., 2014) [[arXiv:1412.4073](#)].
- [65] E.-M. Mueller, F. de Bernardis, R. Bean, and M. Niemack, *Constraints on gravity and dark energy from the pairwise kinematic Sunyaev-Zeldovich effect*, *ArXiv e-prints* (Aug., 2014) [[arXiv:1408.6248](#)].

- [66] A. Kashlinsky, F. Atrio-Barandela, D. Kocevski, and H. Ebeling, *A Measurement of Large-Scale Peculiar Velocities of Clusters of Galaxies: Results and Cosmological Implications*, *ApJ* **686** (Oct., 2008) L49–L52, [[arXiv:0809.3734](#)].
- [67] P. Zhang, *The dark flow induced small-scale kinetic Sunyaev-Zel'dovich effect*, *MNRAS* **407** (Sept., 2010) L36–L40, [[arXiv:1004.0990](#)].
- [68] A. Kashlinsky, F. Atrio-Barandela, and H. Ebeling, *Measuring the Dark Flow with Public X-ray Cluster Data*, *ApJ* **732** (May, 2011) 1, [[arXiv:1012.3214](#)].
- [69] Z. Li, P. Zhang, and X. Chen, *Anomalous Anisotropic Cross-correlations between WMAP CMB Maps and SDSS Galaxy Distribution and Implications on the Dark Flow Scenario*, *ApJ* **758** (Oct., 2012) 130, [[arXiv:1209.0520](#)].
- [70] G. Lavaux, N. Afshordi, and M. J. Hudson, *First measurement of the bulk flow of nearby galaxies using the cosmic microwave background*, *MNRAS* **430** (Apr., 2013) 1617–1635, [[arXiv:1207.1721](#)].
- [71] F. Atrio-Barandela, A. Kashlinsky, H. Ebeling, D. J. Fixsen, and D. Kocevski, *Probing the Dark Flow signal in WMAP 9 yr and PLANCK cosmic microwave background maps*, *ArXiv e-prints* (Nov., 2014) [[arXiv:1411.4180](#)].
- [72] Planck Collaboration, P. A. R. Ade, N. Aghanim, M. Arnaud, M. Ashdown, J. Aumont, C. Baccigalupi, A. Balbi, A. J. Banday, R. B. Barreiro, E. Battaner, K. Benabed, A. Benoit-Lévy, J.-P. Bernard, M. Bersanelli, P. Bielewicz, I. Bikmaev, J. Bobin, J. J. Bock, A. Bonaldi, J. R. Bond, J. Borrill, F. R. Bouchet, C. Burigana, R. C. Butler, P. Cabella, J.-F. Cardoso, A. Catalano, A. Chamballu, L.-Y. Chiang, G. Chon, P. R. Christensen, D. L. Clements, S. Colombi, L. P. L. Colombo, B. P. Crill, F. Cuttaia, A. Da Silva, H. Dahle, R. D. Davies, R. J. Davis, P. de Bernardis, G. de Gasperis, G. de Zotti, J. Delabrouille, J. Démoclès, J. M. Diego, K. Dolag, H. Dole, S. Donzelli, O. Doré, U. Dörl, M. Douspis, X. Dupac, T. A. Enßlin, F. Finelli, I. Flores-Cacho, O. Forni, M. Frailis, M. Frommert, S. Galeotta, K. Ganga, R. T. Génova-Santos, M. Giard, G. Giardino, J. González-Nuevo, A. Gregorio, A. Gruppuso, F. K. Hansen, D. Harrison, C. Hernández-Monteagudo, D. Herranz, S. R. Hildebrandt, E. Hivon, W. A. Holmes, W. Hovest, K. M. Huffenberger, G. Hurier, T. R. Jaffe, A. H. Jaffe, J. Jasche, W. C. Jones, M. Juvela, E. Keihänen, R. Keskitalo, I. Khamitov, T. S. Kisner, J. Knoche, M. Kunz, H. Kurki-Suonio, G. Lagache, A. Lähteenmäki, J.-M. Lamarre, A. Lasenby, C. R. Lawrence, M. Le Jeune, R. Leonardi, P. B. Lilje, M. Linden-Vørnle, M. López-Caniego, J. F. Macías-Pérez, D. Maino, D. S. Y. Mak, N. Mandolesi, M. Maris, F. Marleau, E. Martínez-González, S. Masi, S. Matarrese, P. Mazzotta, A. Melchiorri, J.-B. Melin, L. Mendes, A. Mennella, M. Migliaccio, S. Mitra, M.-A. Miville-Deschênes, A. Moneti, L. Montier, G. Morgante, D. Mortlock, A. Moss, D. Munshi, J. A. Murphy, P. Naselsky, F. Nati, P. Natoli, C. B. Netterfield, H. U. Nørgaard-Nielsen, F. Noviello, D. Novikov, I. Novikov, S. Osborne, L. Pagano, D. Paoletti, O. Perdereau, F. Perrotta, F. Piacentini, M. Piat, E. Pierpaoli, D. Pietrobon, S. Plaszczynski, E. Pointecouteau, G. Polenta, L. Popa, T. Poutanen, G. W. Pratt, S. Prunet, J.-L. Puget, S. Puisieux, J. P. Rachen, R. Rebolo, M. Reinecke, M. Remazeilles, C. Renault, S. Ricciardi, M. Roman, J. A. Rubiño-Martín, B. Rusholme, M. Sandri, G. Savini, D. Scott, L. Spencer, R. Sunyaev, D. Sutton, A.-S. Suur-Uski, J.-F. Sygnet, J. A. Tauber, L. Terenzi, L. Toffolatti, M. Tomasi, M. Tristram, M. Tucci, L. Valenziano, J. Valiviita, B. Van Tent, P. Vielva, F. Villa, N. Vittorio, L. A. Wade, N. Welikala, D. Yvon, A. Zacchei, J. P. Zibin, and A. Zonca, *Planck intermediate results. XIII. Constraints on peculiar velocities*, *AAP* **561** (Jan., 2014) A97, [[arXiv:1303.5090](#)].
- [73] J. Goodman, *Geocentrism reexamined*, *PRD* **52** (Aug., 1995) 1821–1827, [[astro-ph/9506068](#)].
- [74] P. Zhang and A. Stebbins, *Confirmation of the Copernican Principle at Gpc Radial Scale and above from the Kinetic Sunyaev-Zel'dovich Effect Power Spectrum*, *Physical Review Letters* **107** (July, 2011) 041301, [[arXiv:1009.3967](#)].

- [75] U.-L. Pen and P. Zhang, *Observational consequences of dark energy decay*, *PRD* **89** (Mar., 2014) 063009, [[arXiv:1202.0107](#)].
- [76] M. Kamionkowski and A. Loeb, *Getting around cosmic variance*, *Phys.Rev.* **D56** (1997) 4511–4513, [[astro-ph/9703118](#)].
- [77] J. Shao, P. Zhang, W. Lin, Y. Jing, and J. Pan, *Kinetic Sunyaev-Zel'dovich tomography with spectroscopic redshift surveys*, *MNRAS* **413** (May, 2011) 628–642, [[arXiv:1004.1301](#)].
- [78] A. H. Guth and E. J. Weinberg, *Could the Universe Have Recovered from a Slow First Order Phase Transition?*, *Nucl. Phys.* **B212** (1983) 321.
- [79] A. L. Erickcek, S. M. Carroll, and M. Kamionkowski, *Superhorizon perturbations and the cosmic microwave background*, *PRD* **78** (Oct., 2008) 083012, [[arXiv:0808.1570](#)].
- [80] R. K. Sachs and A. M. Wolfe, *Perturbations of a Cosmological Model and Angular Variations of the Microwave Background*, *ApJ* **147** (Jan., 1967) 73.
- [81] L. P. Grishchuk and I. B. Zeldovich, *Long-wavelength perturbations of a Friedmann universe, and anisotropy of the microwave background radiation*, *Soviet Astronomy* **22** (Apr., 1978) 125–129.
- [82] M. S. Turner, *Tilted Universe and other remnants of the preinflationary Universe*, *PRD* **44** (Dec., 1991) 3737–3748.
- [83] M. Bruni and D. H. Lyth, *Peculiar velocity, cosmic perturbation theory and the cosmic microwave background anisotropy*, *Physics Letters B* **323** (Mar., 1994) 118–123, [[astro-ph/9307036](#)].
- [84] E. George, C. Reichardt, K. Aird, B. Benson, L. Bleem, et al., *A measurement of secondary cosmic microwave background anisotropies from the 2500-square-degree SPT-SZ survey*, [arXiv:1408.3161](#).
- [85] P. Zhang and U.-L. Pen, *Deprojecting Sunyaev-Zeldovich Statistics*, *ApJ* **549** (Mar., 2001) 18–27, [[astro-ph/0007462](#)].
- [86] S. Ho, S. Dedeo, and D. Spergel, *Finding the Missing Baryons Using CMB as a Backlight*, *ArXiv e-prints* (Mar., 2009) [[arXiv:0903.2845](#)].
- [87] J. Shao, P. Zhang, W. Lin, and Y. Jing, *The Thermal Sunyaev-Zel'dovich Tomography*, *ApJ* **730** (Apr., 2011) 127, [[arXiv:0903.5317](#)].
- [88] LSST Science Collaboration, P. A. Abell, J. Allison, S. F. Anderson, J. R. Andrew, J. R. P. Angel, L. Armus, D. Arnett, S. J. Asztalos, T. S. Axelrod, and et al., *LSST Science Book, Version 2.0*, *ArXiv e-prints* (Dec., 2009) [[arXiv:0912.0201](#)].
- [89] PRISM Collaboration, P. André, C. Baccigalupi, A. Banday, D. Barbosa, B. Barreiro, J. Bartlett, N. Bartolo, E. Battistelli, R. Battye, G. Bendo, A. Benoît, J.-P. Bernard, M. Bersanelli, M. Béthermin, P. Bielewicz, A. Bonaldi, F. Bouchet, F. Boulanger, J. Brand, M. Bucher, C. Burigana, Z.-Y. Cai, P. Camus, F. Casas, V. Casasola, G. Castex, A. Challinor, J. Chluba, G. Chon, S. Colafrancesco, B. Comis, F. Cuttaia, G. D'Alessandro, A. Da Silva, R. Davis, M. de Avillez, P. de Bernardis, M. de Petris, A. de Rosa, G. de Zotti, J. Delabrouille, F.-X. Désert, C. Dickinson, J. M. Diego, J. Dunkley, T. Enßlin, J. Errard, E. Falgarone, P. Ferreira, K. Ferrière, F. Finelli, A. Fletcher, P. Fosalba, G. Fuller, S. Galli, K. Ganga, J. García-Bellido, A. Ghribi, M. Giard, Y. Giraud-Héraud, J. Gonzalez-Nuevo, K. Grainge, A. Gruppuso, A. Hall, J.-C. Hamilton, M. Haverkorn, C. Hernandez-Monteagudo, D. Herranz, M. Jackson, A. Jaffe, R. Khatri, M. Kunz, L. Lamagna, M. Lattanzi, P. Leahy, J. Lesgourgues, M. Liguori, E. Liuzzo, M. Lopez-Caniago, J. Macias-Perez, B. Maffei, D. Maino, A. Mangilli, E. Martinez-Gonzalez, C. Martins, S. Masi, M. Massardi, S. Matarrese, A. Melchiorri, J.-B. Melin, A. Mennella, A. Mignano, M.-A. Miville-Deschênes, A. Monfardini, A. Murphy, P. Naselsky, F. Nati, P. Natoli, M. Negrello, F. Noviello, C. O'Sullivan, F. Paci,

- L. Pagano, R. Paladino, N. Palanque-Delabrouille, D. Paoletti, H. Peiris, F. Perrotta, F. Piacentini, M. Piat, L. Piccirillo, G. Pisano, G. Polenta, A. Pollo, N. Ponthieu, M. Remazeilles, S. Ricciardi, M. Roman, C. Rosset, J.-A. Rubino-Martin, M. Salatino, A. Schillaci, P. Shellard, J. Silk, A. Starobinsky, R. Stompor, R. Sunyaev, A. Tartari, L. Terenzi, L. Toffolatti, M. Tomasi, N. Trappe, M. Tristram, T. Trombetti, M. Tucci, R. Van de Weijgaert, B. Van Tent, L. Verde, P. Vielva, B. Wandelt, R. Watson, and S. Withington, *PRISM (Polarized Radiation Imaging and Spectroscopy Mission): An Extended White Paper*, *ArXiv e-prints* (Oct., 2013) [[arXiv:1310.1554](#)].
- [90] **Topical Conveners: J.E. Carlstrom, A.T. Lee** Collaboration, K. Abazajian et al., *Inflation Physics from the Cosmic Microwave Background and Large Scale Structure*, *Astropart.Phys.* **63** (2015) 55–65, [[arXiv:1309.5381](#)].
- [91] B. C. Friedman, A. Cooray, and A. Melchiorri, *WMAP-normalized Inflationary Model Predictions and the Search for Primordial Gravitational Waves with Direct Detection Experiments*, *Phys.Rev.* **D74** (2006) 123509, [[astro-ph/0610220](#)].
- [92] S. Dodelson, *Modern cosmology*. Academic Press, 2003.
- [93] U. Seljak and M. Zaldarriaga, *A Line-of-Sight Integration Approach to Cosmic Microwave Background Anisotropies*, *ApJ* **469** (Oct., 1996) 437, [[astro-ph/9603033](#)].
- [94] P. Zhang, *Exact analytical solution of the linear structure growth rate in Λ CDM cosmology and its cosmological applications*, *PRD* **83** (Mar., 2011) 063510, [[arXiv:1101.5164](#)].
- [95] S. M. Carroll, W. H. Press, and E. L. Turner, *The cosmological constant*, *Annual Review of Astronomy & Astrophysics* **30** (1992) 499–542.